



# Magma decompression rate calculations with EMBER: A user-friendly software to model diffusion of H<sub>2</sub>O, CO<sub>2</sub> and S in melt embayments

Guillaume Georgeais, Kenneth T. Koga, Yves Moussallam, Estelle F.  
Rose-Koga

## ► To cite this version:

Guillaume Georgeais, Kenneth T. Koga, Yves Moussallam, Estelle F. Rose-Koga. Magma decompression rate calculations with EMBER: A user-friendly software to model diffusion of H<sub>2</sub>O, CO<sub>2</sub> and S in melt embayments. *Geochemistry, Geophysics, Geosystems*, 2021, 10.1029/2020GC009542 . hal-03265994

**HAL Id: hal-03265994**

**<https://uca.hal.science/hal-03265994>**

Submitted on 21 Jun 2021

**HAL** is a multi-disciplinary open access archive for the deposit and dissemination of scientific research documents, whether they are published or not. The documents may come from teaching and research institutions in France or abroad, or from public or private research centers.

L'archive ouverte pluridisciplinaire **HAL**, est destinée au dépôt et à la diffusion de documents scientifiques de niveau recherche, publiés ou non, émanant des établissements d'enseignement et de recherche français ou étrangers, des laboratoires publics ou privés.



Distributed under a Creative Commons Attribution 4.0 International License

# Magma decompression rate calculations with EMBER: A user-friendly software to model diffusion of H<sub>2</sub>O, CO<sub>2</sub> and S in melt embayments

Guillaume Georgeais<sup>1</sup>, Kenneth T. Koga<sup>1</sup>, Yves Moussallam<sup>2,3</sup>, Estelle F. Rose-Koga<sup>1</sup>

<sup>1</sup>*Université Clermont Auvergne, CNRS, IRD, OPGC, Laboratoire Magmas et Volcans, F-63000 Clermont-Ferrand, France*

<sup>2</sup>*Lamont-Doherty Earth Observatory, Columbia University, New York, NY 10027, USA*

<sup>3</sup>*Department of Earth and Planetary Sciences, American Museum of Natural History, New York, NY 10024, USA*

Corresponding author: Guillaume Georgeais; [guillaume.georgeais@uca.fr](mailto:guillaume.georgeais@uca.fr)

**Keywords:** volcanic eruption, magma degassing, conduit processes, volatile element exsolution, GUI

## Highlights:

- EMBER is a new, freely available, GUI software that models magma ascent rates for basalt to rhyolite with H<sub>2</sub>O, CO<sub>2</sub> and S diffusion profiles
- EMBER was validated by reproducing previous published literature data
- For mafic eruptions, we found a notable correlation between maximum recalculated decompression rates and eruption magnitude or plume height

## ABSTRACT

Magma decompression rate is one of the most important parameters in controlling eruption dynamics. One way to determine decompression rate is by fitting a volatile elements diffusion profile to a concentration gradient in crystal-hosted embayments. Previous studies have used a variety of diffusion models, limiting the possibility for inter-study comparison. Here, we introduce EMBER (EMBayment-Estimated Rates), a standalone versatile tool that models diffusion of volatile elements along melt embayments. Our model relies on the *pdepe* function of MATLAB to calculate diffusion profiles of H<sub>2</sub>O, CO<sub>2</sub> and S through the finite difference method. EMBER uses a grid search seeking out the best fits for decompression rates, initial dissolved concentration of each studied volatile and initial exsolved gas content, while setting three constants: temperature along the ascent and pressure at the beginning and end of the ascent. Our model can compute the rate for basaltic, intermediate, and rhyolitic compositions. We applied EMBER to previous studies to evaluate and validate our model. We then re-processed "homogeneously" the raw data from the literature for a comparison. In other words, the same protocol was used for each diffusion profiles removing the literature-specific strategies used to constrain unknown parameters. With this comparison, we found a statistically significant positive correlation between maximum magma decompression rates and explosivity of the related eruption. EMBER is expected to help increase the number of volatile diffusion in embayments studies aiming at constraining magma decompression and ascent rates and to facilitate inter-study comparisons.

## 1. INTRODUCTION

Magma ascent rate is a fundamental physical parameter in determining the behavior of a volcanic eruption. Magma ascent rate can be estimated in several ways, during ascent and eruption by geophysical methods, or after the eruption using geochemical and petrological methods. One example of a geophysical method is the analysis of volcanic earthquakes, in which the progressive migration of tremors from a depth to the surface is interpreted as the upward migration of ascending magma [e.g., Aki and Koyanagi., 1981; Scandone and Malone., 1985; Klein et al., 1987; Tryggvason., 1994]. Geochemical methods to determine magma ascent rate are numerous but most of them are only applicable to limited melt compositions. In andesitic magma for instance, the thickness of amphibole breakdown rims has been used to determine ascent rates based on the experimentally-determined rate of the break-down reaction [e.g., Carey and Sigurdsson., 1985; Rutherford and Hill., 1993; Geschwind and Rutherford., 1995; Browne and Gardner., 2006]. Another example is the use of diffusion profiles (e.g., Fe-Mg or H<sub>2</sub>O) at the rims of minerals in mantle xenoliths as they re-equilibrate with their carrier melt on their way to the surface [e.g., Mackwell and Kohlstedt., 1990; Klügel et al., 1997; Klügel., 1998; Kohlstedt and Mackwell., 1998; Le Voyer et al., 2014]. Knowing the diffusion coefficient of the species of interest, one can derive an estimate of the magma ascent rate for these eruptions [e.g., Demouchy and Mackwell., 2006; Sparks et al., 2006; Rutherford., 2008]. Another method, based on nucleation theory, links the bubble number density in erupted products (measurable from 2D and 3D observations) to the magma decompression rate [Toramaru., 1989, 1995, 2006]. This theoretical relationship has been reproduced experimentally but is not applicable to natural samples, once bubbles start to coalesce [e.g., Martel and Iacono-Marziano., 2015].

One method, which holds the potential to be widely applicable for a wide range of magma compositions and decompression rates, is the analysis of the diffusion profiles of

volatile elements along melt embayments (also called re-entrants). Embayments are crystal-hosted elongated melt pockets of various shapes and sizes, opened to the outside melt [e.g., Anderson., 1991]. Their formation mechanism is similar to that of melt inclusions [e.g., Faure and Schiano., 2005], through either crystallization around a defect or dissolution of the host crystal, with the exception that they remain connected to the surrounding bubbly melt. They have been studied in quartz [e.g., Liu et al., 2007; Myers et al., 2018], in plagioclases [e.g., Humphreys et al., 2008] and olivine crystals [e.g., Lloyd et al., 2014; Ferguson et al., 2016; Moussallam et al., 2019], in quenched material ranging from basalt to rhyolite in composition. During magma ascent, the volatile content of the melt surrounding the embayment will decrease, maintaining equilibrium with the exsolved gas phase. The limited volume of melt embayments, however, often prevents bubble formation inside, resulting in embayment melt being super-saturated in volatiles compared to the surrounding melt. This difference in chemical potential leads to a concentration gradient and to diffusive transport of volatile species from the interior to the mouth of the embayment resulting in a diffusion profile. If such a profile is preserved in natural samples, it can then be inverted to derive a decompression rate assuming that the elongated tubular shape of the embayment and the relative impermeability of the host crystal led to unidirectional (1D) diffusion and prevented any advective melt motion in the embayment. The dependency of volatile diffusion in embayments on multiple parameters (melt composition, temperature, pressure, degassing path, decompression rate) makes the interpretation of natural diffusion profiles a challenging endeavour. A numerical model adapted to a wide range of magma compositions is therefore needed to generate multiple diffusion profiles with known parameters and find the synthetic profile which most closely reproduces the measurement.

## 1.1 Existing embayment volatile diffusion models

Several such numerical models have been developed in the last decades (Table 1). The first published code was developed in FORTRAN 77 [Liu et al., 2007]. Assuming a certain temperature, pressure, initial concentration, exsolved gas, degassing path and decompression rate, the code generated time-dependent profiles of H<sub>2</sub>O and CO<sub>2</sub> concentrations until the fragmentation pressure is reached. The process was repeated several times with different decompression rates to find the best fit. A second model was presented by Humphreys et al., [2008] using the COMSOL multiphysics software to model only H<sub>2</sub>O profiles. Their model imposes the final concentration at the mouth of the embayment from the start of the calculation and allows the software to run the diffusion calculation. Lloyd et al., [2014] developed a model calculating simultaneously, for a range of decompression rates, three volatile element profiles at once: H<sub>2</sub>O, CO<sub>2</sub> and S. In a following study, an improved development of a MATLAB code by Ferguson et al., [2016] took H<sub>2</sub>O, CO<sub>2</sub> and S into account and considered not only a range of decompression rates but also the initial concentration of each volatile element as well as the exsolved gas content at the beginning of the ascent ( $M_0$ ) for basaltic compositions. The addition of this new parameter: ( $M_0$ ), the pre-existing (already exsolved volatile content in equilibrium with magma at the onset of a magma ascent), proved to have a significant impact on the modelled profile and made the grid search more complex and the result better constrained [Ferguson et al., 2016]. Another study subsequently build the FORTRAN 77 model from Liu et al., [2007] in MATLAB with updated diffusion coefficients for rhyolitic compositions and a best fit search algorithm [Myers et al., 2018]. This code was later updated taking the pressure at which degassing stops as a free parameter [Myers et al., 2021]. Another code, written in Rstudio and restricted to basaltic melts, took into account all the aforementioned parameters with fixed inputs and was made openly available [Moussallam et al., 2019]. One of the most recent model is tuned to intermediate magma compositions, contains a specific S solubility relation and a general H<sub>2</sub>O

diffusion coefficient relation for intermediate magma, and looks for the decompression rate and initial pressure [Newcombe et al., 2020]. The latest model to date is written in Matlab and uses grid searches to find decompression rate, initial concentration of H<sub>2</sub>O and S and exsolved gas content [Moussallam et al., 2021].

At present, seven different data processing methods to model volatile diffusion profiles in embayments exist; each published study uses its specific model written on four different platforms (FORTRAN 77, COMSOL, MATLAB and RStudio). Other than the code of Moussallam et al., [2019], none are directly downloadable without a specific request to the authors. Each code considers different input parameters, different volatile species and is tuned to a specific melt composition. This lack of consistency is an issue for inter-study comparison and the lack of open software access can be an impediment to a large number of new studies on natural products.

The aim of this article is to provide the community with a user-friendly and cross-operating system MATLAB code that is able to constrain decompression rates from volatile diffusion in melt embayments for rhyolitic to basaltic melt compositions, and for as wide a range of starting conditions as possible. We then retroactively analyze all volatile diffusion profiles from the literature using EMBER. Our results help identify potential discrepancies in published decompression rates, notably for the Mt St Helens 1980's eruption, and provide an easily comparable, self-consistent summary of decompression rates obtained from volatile element diffusion in melt embayments published to date. Our software, EMBER, calculates results likely comparable to those by the DIPRA software [Girona and Costa., 2013], which can extract timescales from diffusion zoning in olivine crystals, and is also a widely distributed MATLAB program.

## 2. Code architecture

### 2.1 Diffusion model

Volatile element diffusion in embayments can be regarded as a 1D process, because of their elongated, tube-like geometries and the incompatibility of the elements in their mineral host [Ferguson et al., 2016; Humphreys et al., 2008; Liu et al., 2007; Lloyd et al., 2014; Moussallam et al., 2019, 2021; Myers et al., 2018, 2021; Newcombe et al., 2020]. While this is a commonly accepted assumption, further studies are needed to assess the impacts of the three-dimensional shape of embayments to volatiles diffusion [deGraffenried and Shea., 2020]. If it proves to be relevant, EMBER will need to be updated accordingly to compute both 1D and 3D diffusion. The evolution of the concentration gradient is therefore described by Fick's Second Law (Eq.1):

$$\frac{\partial C}{\partial t} = \frac{\partial}{\partial x} \left( D(x, t) \frac{\partial C}{\partial x} \right) \quad (1)$$

$$C = C_i \text{ at } x > 0, t = 0 \quad (2)$$

$$C = C_{sat}(t) \text{ at } x = 0, t > 0 ; \frac{dC}{dx} = 0 \text{ at } x = X, t > 0 \quad (3)$$

where  $D$  is the diffusion coefficient of the studied volatile species;  $C$ , the concentration of studied species,  $x$ , the distance from the mouth of the embayment,  $X$ , the distance at the interior of the embayment,  $C_{sat}$ , the saturation concentration calculated at the mouth of the embayment by using a solubility model,  $C_i$ , the initial concentration along the embayment and  $t$ , the time. These diffusion equations show that diffusion coefficients depend heavily on  $H_2O$  concentration ( $C_{H_2O}$ ), temperature and pressure. These three parameters, and therefore the diffusion coefficient, all change during ascent. Diffusion coefficients are hence calculated along every point of the embayment from the start to the end of the calculation.

The boundary condition at the interior is defined by an absence of mass flux (Neumann condition) (Eq.2) and the volatile concentration at the mouth of the embayment is fixed but varies with respect to time  $t$  (Dirichlet boundary condition). The initial volatile concentration  $C_{init}$  along the embayment is constant, and the value should be the concentrations of volatile elements at the initiation of magma ascent. Volatile concentration at the mouth of the embayment is set by the solubility of each volatile species along a pressure related path of the magma ascent, and these constraints are entered into EMBER as a text file. For example, EMBER's default setup reads output files from SolEx [Witham et al., 2012], and VolatileCalc [Newman and Lowenstern., 2002] depending on magma types.

Solubility of gas species depends on  $T$ ,  $P$ , magma composition and exsolved gas content ( $M_0$ ). EMBER does not calculate the solubility of volatiles and uses an "external" solubility model like VolatileCalc [Newman and Lowenstern., 2002], SolEx [Witham et al., 2012] or any other model that the user chooses to calculate the degassing paths. Since the value of  $M_0$  is initially unknown, a typical calculation is done by choosing a "target exsolved gas content" thus by setting a corresponding degassing path. EMBER works with seven solubility files accounting for  $M_0$  values of 0, 0.1, 0.2, 0.4, 0.8, 1.6, 3.2 wt. %, which are supplied by the user. EMBER interpolates those seven degassing paths to find the degassing path associated with the targeted exsolved gas content. It should be noted that, when VolatileCalc-generated degassing paths are used, EMBER imposes the reference point concentrations of 0.01wt. %  $H_2O$ , 1 ppm  $CO_2$  and 1 ppm S at  $P=1$  bar because VolatileCalc does not model the degassing path down to one bar.

EMBER calculates all model diffusion profiles of the volatile elements following the grid search which range is defined by the user, before iteratively comparing measured and calculated profiles. First, profiles are calculated by varying three parameters for each calculation loop: constant decompression rate, initial volatile content and exsolved gas

content, for each element. Parameters such as temperature, melt composition, initial pressure prior to ascent and pressure at which decompression stops are specified together with the volatile species of interest ( $H_2O$ ,  $CO_2$ , S) and they are fixed for all calculations. The program calculates diffusion profiles using finite difference formulation solved with the *pdepe* function, an ordinary differential equation (ODE) solver from MATLAB.

Diffusion coefficients used in the model calculations are based on the following equations and calculated for each step of the ascent and at each point of a given profile. Water diffusion coefficient ( $D_{H_2O}$ ) in  $m^2 \cdot s^{-1}$  for basaltic melt is given by

$$D_{H_2O} = \exp[-11.924 - 1.003 \ln(C_{H_2O})] * \exp\left[\frac{-\exp(11.836 - 0.139 \ln(C_{H_2O}))}{RT}\right] \quad (4)$$

where  $C_{H_2O}$  is water concentration in wt. %; R, the gas constant in  $J \cdot mol^{-1} \cdot K^{-1}$  and T, the temperature in Kelvin [Freda et al., 2003]. For melt with intermediate composition ( $55 < SiO_2 < 70$  wt. %), the water diffusion coefficient ( $D_{H_2O_t}$  in  $m^2 \cdot s^{-1}$ ) is calculated using a combination of equations (5a-i), from Ni and Zhang., [2018], as previously used by Newcombe et al., [2020]:

$$D_{H_2O_t} = D_{H_2O_m} \left(1 - \frac{dX_{OH}}{2dX}\right) + D_{OH} \frac{dX_{OH}}{2dX}, \quad (5a)$$

$$D_{H_2O_m} = D_0 \exp(aX), \quad (5b)$$

$$D_{OH} = const, \quad (5c)$$

$$\frac{dX_{OH}}{2dX} = \frac{1-2X}{\sqrt{4X(X-1)\left(1-\frac{4}{K}\right)+1}}, \quad (5d)$$

$$\ln K = 2.6Y_{SI} - \frac{4339Y_{SI}}{T}, \quad (5e)$$

$$a = -94.07 + 74.112Y_{SI} + \frac{198508 - 166674Y_{SI}}{T}, \quad (5f)$$

$$\ln D_{OH} = -16.78 - 37.428Y_{SI} - \frac{39250 - 27576Y_{SI}}{T}, \quad (5g)$$

$$\ln \left( \frac{D_{OH}}{D_0} \right) = -56.09 - 115.93Y_{SI} + 160.54\sqrt{Y_{SI}} - \frac{3970\sqrt{Y_{SI}}}{T}, \quad (5h)$$

$$\ln D_0 = 8.02 - 31Y_{SI} + 2.348PY_{SI} + \frac{121824Y_{SI} - 118323\sqrt{Y_{SI}} - (10016Y_{SI} - 3648)P}{T}, \quad (5i)$$

with  $Y_{SI}$ , the mole fraction of Si among all cations,  $D_0$ , a diffusion parameter in  $m^2 \cdot s^{-1}$ ,  $K$ , the equilibrium constant,  $X$ , the mole fraction of each species,  $P$  in GPa,  $T$  in Kelvin,  $a$ , a dimensionless parameter,  $D_{OH}$  the OH diffusivity in  $m^2 \cdot s^{-1}$ ,  $D_{H_2O_m}$ , the molecular  $H_2O$  diffusivity in  $m^2 \cdot s^{-1}$  and  $D_{H_2O_t}$ , the total  $H_2O$  diffusivity in  $m^2 \cdot s^{-1}$ .

For rhyolitic melt, the water diffusion coefficient (in  $\mu m^2 \cdot s^{-1}$ ) is given by,

$$D_{H_2O} = C_{H_2O} \exp(10.49 - \frac{10.661}{T} - \frac{1.772P_t}{T}) \quad (6a)$$

for low ( $\leq 2$  wt. %) water melt, where  $P_t$  is the pressure in MPa at time  $t$  [Zhang and Behrens., 2000]. However, if the water content is high (from 2 to 8 wt. %), diffusion coefficient is calculated by,

$$D_{H_2O} = X \exp(m) \left\{ 1 + \exp \left[ 56 + m + X \left( -34.1 + \frac{44620}{T} + \frac{57.3P_t}{T} \right) - \sqrt{X} \left( 0.091 + \frac{4.77 \cdot 10^6}{T^2} \right) \right] \right\} \quad (6b)$$

where  $m = -20.79 - 5030/T - 1.4 P_t/T$ , and  $X = (C_{H_2O}/18.015) / [C_{H_2O}/18.015 + (100 - C_{H_2O})/32.49]$  [Zhang and Behrens., 2000]. The diffusion coefficient of  $CO_2$  ( $D_{CO_2}$ ), in  $m^2 \cdot s^{-1}$ , is given by,

$$D_{CO_2} = \exp \left[ -14.34 - \frac{17360 - 0.6527P_t}{T} + \left( -0.7171 + \frac{1436.8}{T} \right) C_{H_2O} \right] \quad (7)$$

for basalts to rhyolites [Nowak et al., 2004; Zhang et al., 2007]. The program also calculates diffusion coefficient of S ( $D_S$ ), in  $m^2.s^{-1}$  :

$$D_S(i) = \exp\left(-8.21 - \frac{27692 - 651.6 C_{H_2O}}{T}\right) \quad (8)$$

[Zhang et al., 2007]. It is to be noted that the sulfur diffusivity determined by Zhang et al., [2007] is applicable only to basaltic melts under reduced conditions [Zhang et al., 2007].

## 2.2 Best fit determination

The second part of the code compares a measured concentration profile to a series of calculated ones (with N set of parameters) to find the best fit and its associated parameters (i.e. grid search). EMBER favours the grid search over other more efficient optimization methods (e.g. gradient search method), because with the mixture of diffusion of dissimilar species, it is not clear *a priori* if there will always exist a unique solution. While computationally intensive (and inefficient), we consider it is more suitable to take an approach of “calculate-all”. The best fit is determined by comparing the dimensionless normalized residual square error ( $NErr_j$ ) for each  $j$  of N sets of parameters,

$$NErr_j = \sum_i \frac{1}{u_j^2} (C_{ij} - Cs_{ij})^2 \quad (9)$$

where  $u_j$  is the analytical measurement uncertainty applied at the highest volatile concentration measured in the embayment; usually at the interior of the embayment (i.e: an uncertainty of 5% of  $Cs_{ij\_max}$ ),  $i$  denotes discrete points along the distance to the embayment mouth,  $C_{ij}$  is the calculated concentration and  $Cs_{ij}$  is the measured concentration. Among the generated profiles, the one that gives the minimum  $NErr_j$  is the best fit. One may calculate  $NErr_j$  by considering the “weighting and scaling of the error” of each volatile (further details can be found in part 4.5). By doing so, the program first calculates  $NErr_j$  values without

dimensions thanks to  $u_j$ . The term  $u_j$  effectively constrains the “weight” of three diffusion profiles ( $H_2O$ ,  $CO_2$ , and  $S$ ) as measurements with better uncertainty (in relative term) have a stronger influence to the sum total of three  $NErr$ . EMBER then scales the  $NErr$  values between each volatiles before adding them. If one chooses not to weight and scale each volatile species’ error,  $u_j = 1$ .

EMBER assesses statistical variations of  $NErr$  by a Monte Carlo simulation accounting for the uncertainty of the measurement  $C \pm \sigma$ , using a Gaussian distribution random function to generate  $m$  iterations of possible profiles within measurement uncertainties. Therefore, for a parameter set (*i.e.* case  $j$ ), there is  $m$  number of  $NErr$  computed by comparing a calculated profile against  $m$  numbers of the randomly generated profiles  $Cs_i + \varepsilon$  (Figure 1, Step 1). A similar approach is taken for the uncertainty of  $\chi$ . The result of this simulation is represented by a mean ( $Nerr\_m$ ) and its related 1- $\sigma$  confidence interval for a parameter set  $j$  (Figure 1, Step 2).

### 2.3 Propagation of errors

The uncertainties on the fit parameters  $C_i$ ,  $dPdt$  and  $M_0$  (to a lesser extent) are assessed by the statistical distributions of the parameters that are extracted from the calculated profiles  $y$  that satisfy the following condition (Figure 1. Step 3):

$$\Pr(a - \sigma_1 \leq y \leq a + \sigma_2) = 68\% \quad (10)$$

Here,  $a$  is the value for which  $Nerr\_m$  is the smallest, and  $\sigma_1$  and  $\sigma_2$  respectively the lower and upper boundaries of the confidence interval, calculated using the *prctile* MATLAB function. For every  $j$  calculated profiles (with a set of parameters), there is a corresponding  $NErr$ . Equation (10) states that there are cases of calculated profiles for which  $NErr$  is within the expected uncertainty. EMBER extracts the corresponding parameters ( $dPdt$  and  $C_i$ ) and

report the distribution of values as mean and 1- $\sigma$  confidence interval, which are the best fit parameter and an associated uncertainty (Figure 1. Step 4 and 5). In consequence, measurement uncertainties must be entered by the user in EMBER because of the Monte Carlo error propagation. An uncertainty on the distance between two measurement spots is set by default at  $\pm 2 \mu\text{m}$  and can be changed to whichever value the user requires, down to  $0 \mu\text{m}$  if needed.

### **3. Examples of model outputs**

#### **3.1 Organization of the graphical user interface**

EMBER runs inside a user-friendly Graphical User Interface (GUI) upon execution of the application file. The GUI is separated in two parts: the input section, dedicated to generating the grid search and decompression conditions (left hand side Part1, panels a, b, c; Fig.2), and the results section dedicated to displaying the results once calculation is terminated (Part 2, panels a, b; Fig. 2). Panel 2c display a process log during the calculations. Figure 3 shows the result of a simulation using the volatile profiles measured in an embayment from the study of Ferguson et al., [2016] as an example. Unticking the “Weighting and scaling of error” checkbox will remove the scaling of NErr. The  $u_j$  parameter from equation (8) is set to 1 in this case and NErr is not scaled before being added for the cumulative error calculation. In such case, as all concentration are treated as weight percent internally, the  $\text{H}_2\text{O}$  profile will usually weight more than the others as it usually records much larger variations in absolute concentration.

#### **3.2 Outputs of the calculation**

Figures generated by EMBER have two purposes: (1) to display the results of the calculation and (2) to track the variation of the best-fit estimation with parameters from the grid search such as  $M_0$  or  $C_i$ . Figure 3a shows the influence of the exsolved gas content to the resulting best-fit diffusion profile. Other parameters can be tested. For example, the number of volatile species fitted at once (single or up to 3, solid line or dashed line, respectively; Fig. 3b) also influences the resulting best-fit profile. Figure 3c shows the sensitivity of the cumulative error over decompression rate and exsolved gas content ( $M_0$ ). Figure 3d shows the influence of the initial concentration on each volatile best fit error calculation.

Each figure generated is saved in a unique file (.fig) directly openable with EMBER. Along with the figures, EMBER also produces four Excel (.xls) files (.csv for Mac). They contain the input parameters, the diffusion profiles of each best case, for every decompression rate with the best  $C_i$  and  $M_0$ , and a copy of the results for each volatile with the respective exsolved gas content.

## **4. Calculation and performance test**

### **4.1 A priori requirements**

As with all computational software, meaningful results in EMBER will only be achieved with appropriate dataset. Investigations should be limited to entirely glassy embayments, sampled from rapidly quenched deposits (e.g., <2 cm sized tephra), exhibiting a geometry that is close to that of a cylinder with constant radius. More complex geometries would void the core assumption of unidirectional diffusion and necessitate 3D diffusion modeling. [e.g., deGraffenried and Shea., 2020], which is not currently supported by EMBER. The longer the embayment, the more likely it is to display a concentration plateau in the diffusion profile indicative of  $C_i$  and the starting pressure of ascent ( $P_{Start}$ ). In absence of such condition, we recommend the user to determine  $P_{Start}$ ,  $C_i$  and  $T$  from melt inclusions and geo-

thermobarometry studies. Finally, volatile concentration measurements on surrounding glass are required to assess  $P_{\text{end}}$ , the pressure of quenching.

While we used VolatileCalc and SolEx as the main degassing path generators in the examples below, it should be noted that EMBER can also read degassing paths from any other software as long as the input files comply with the required format (see the tutorial in the additional instructions). Hence, the choice of degassing path software is ultimately up to the user's preference.

## 4.2 Comparison with previous studies

We re-analysed the natural volatile diffusion profiles in embayments from previous studies, to assess the quality of EMBER's decompression rate calculation: from the 1980 Mt St Helens [Humphreys et al., 2008], 1974 Fuego [Lloyd et al., 2014], 1500, 1650 and 1959 Kīlauea [Ferguson et al., 2016], 27 ka Taupo [Myers et al., 2018], 767 ka Long Valley [Myers et al., 2018], 2 Ma Yellowstone [Myers et al., 2018], 2017-2018 Ambae/Aoba [Moussallam et al., 2019], Late Bronze Age (LBA) Santorini [Myers et al., 2021] and December 2018 Ambrym [Moussallam et al., 2021] eruptions. We used the uncertainties reported in each study when provided. Also when provided, we directly used the specific grid search (e.g. Ferguson et al., [2016] provides a range of  $M_0$ ). Otherwise, we estimated the possible range of grid search from the reported uncertainties for decompression rates and initial concentrations. Degassing paths were calculated respecting P, T, and volatile contents used in the original studies (typically, we use SolEx or VolatileCalc when authors specified it). Similarly, the re-analysed results were calculated using the same set of values for  $M_0$  as the original literature data to which they are compared. In detail this was  $M_0 = 0.1, 1.6, 1.6, 0.8$  wt. % respectively for IkiE1, ReticE1, ReticE2 and KeaE1 [Ferguson et al., 2016],  $M_0 = 0.4, 0, 0, 3.2$  wt. % respectively for AF2, AD5, AE38 and PG11 [Moussallam et al., 2021] and  $M_0 = 0$  wt. % for

all embayments from Ambae [Moussallam et al., 2019]. For all other studies of which the exsolved gas content was not specified we used  $M_0 = 0$  wt. %. In some cases [Myers et al., 2018], we limited our tests to three samples from each investigated eruption, making sure to test the samples with the highest and lowest estimation. All results except those from Ambrym were calculated with the weighting and scaling of the error. The results are shown in Figure 4.

There is a good agreement between EMBER results and most literature values. Data from the 1980's Mt St Helens eruption [Humphreys et al., 2008] show consistent disparity between the published decompression rates and EMBER's. This difference is due to significantly different boundary conditions of this study compared with the original. The model from the original study [Humphreys et al., 2008] fixed the final concentration at the mouth of the embayment, prior to the ascension. Since the diffusion phenomenon is gradient-dependent, imposing a high concentration gradient at the beginning of the simulation should lead to faster volatile diffusion and a higher decompression rate estimation. This is a critical simplification leading to significant differences in the calculated decompression rate. Other minor differences observed between our re-analysis and earlier decompression rates estimates come from (1) the use of a different  $H_2O$  diffusion coefficient as well as a single episode of ascent in all our calculation (as opposed to two-step ascent; [Lloyd et al., 2014]), (2) the calculation of diffusion coefficient (e.g., taking into account the change of diffusivity due to  $H_2O$  diffusion or choosing different equations of diffusivity) and (3) the weighting and scaling of error associated with each volatile diffusion profile in all our calculations (Fig.4).

#### 4.3 Monte Carlo simulation

We ran tests on three samples with variable number of Monte Carlo iterations ( $m=3, 11, 101, 501$  and  $1001$ ) to determine the lowest number of the iterations to achieve stable assessment

of uncertainties: BT251, a rhyolite from Long Valley, ReE2, a reticulite from 1500 CE Kīlauea lava fountain and AO02, a basalt from phase 2 of the 2017-2018 eruption of Ambae. For BT251, the representation gradually acquires the shape of a pseudo-gaussian distribution with increasing iteration counts. The median and mean values of all filtered decompression rate do not change significantly with increasing iterations (Fig 5) and a stability of the data distribution is quickly achieved (for  $m=11$ ). For ReE1, the precision of the nanoSIMS measurements and the low decompression rate leads to a stable calculation and a needle shaped histogram even for  $m=3$ , suggesting that the results are well constrained. For AO02 the shape of the histogram is pointy, unimodal and skewing right with a long tail. With higher  $dP/dt$  values (i.e., sharper diffusion profiles), modelled diffusion profiles become more and more similar, making it harder for the software to find the best solution. This results in a skewed solution histogram with a long tail and a more noticeable difference between mean and median value. For such cases, stability is reached for  $m = 101$ . We recommend 101 iterations (EMBER default iteration value) as it was enough to reach a stable solution for our most uncertain case.

#### 4.4 How well does EMBER constrain $M_0$ ?

Calculation of the exsolved gas content has been introduced within the embayment method with the calculations made by Ferguson et al., [2016]. They noted it had a significant influence on their calculation of decompression rate, which was confirmed by later studies and by EMBER (Fig 3a and Fig 6a). The effect is mostly a result of the exsolved gas content having a large influence on the degassing trend. From our investigation of literature data, we see that a change of  $M_0$  from 0 to 3.2 wt. % can cause the decompression rate estimation to increase by 10 fold (Fig 6 (a)). This variation is most pronounced on  $H_2O$  profiles in embayments of basaltic composition (Fig 6 (a), (b), (c)). Except for these few cases, the

impact of  $M_0$  is hardly significant enough for it to be accurately determined using only diffusion profiles (the associated error frequently covering the entire range studied).

The change of decompression rate in response to variable  $M_0$  illustrates the importance of  $P_{\text{end}}$  (Fig. 6 (d)) (which must be determined from measured data) and the critical influence of the modelled degassing path.

The best fit  $M_0$  values are directly affected by the choice of  $P_{\text{end}}$  (Fig. 6 (d)) which must be determined from measured data. Taking as an example, the calculation of one profile from Ferguson et al., [2016] which ends at a specified quenching pressure  $P_{\text{end}} = 2.75$  MPa. Using the decompression path (from SolEx) for  $M_0 < 1.6$  wt. %, the resulting  $\text{H}_2\text{O}$  concentration at  $P = 2.75$  MPa would be higher than  $C_s(x = 0)$ , the measured concentration at the mouth of the embayment approximated with the glass measurement, by up to 0.20 wt. %. Synthesized diffusion profiles in this case cannot reproduce the concentration at the mouth of the embayment for  $M_0 < 1.6$  wt. %. Because of this limitation, as shown in figure 3a, only a degassing paths associated with at the best fit  $M_0$  value could match the whole diffusion profile by fitting the concentration at the mouth. It should be noted that if a different  $P_{\text{end}}$  is chosen, it is possible that EMBER finds another best-fit  $M_0$  (Fig 6 (d)). Therefore, we advise the user to be cautious when choosing  $P_{\text{end}}$  for decompression rate modelling, especially in case constrained by one volatile species (Fig 6 (e), (f)).

#### 4.5 Weighting and scaling of error

EMBER leaves the user the choice to, or not to, equally weigh and scale the relative contribution of each volatile profile equally, when calculating the cumulative error. For example, the study from Ferguson et al., [2016] gives equal weight ( $u_j = 1$ ) to all three volatile species, except on a few cases. By doing so, the best fit  $N\text{Err}_j$  calculated from  $\text{H}_2\text{O}$

profiles is several orders of magnitude higher than the best fit  $NErr_j$  calculated for CO<sub>2</sub> or S profiles. That difference is due to the range of concentration variation, as H<sub>2</sub>O usually varies within a few wt. % and CO<sub>2</sub> and S usually varies within thousands of ppm at best. Cumulative error calculation, and subsequently the best fit determination, becomes heavily dependent on the H<sub>2</sub>O  $NErr_j$  value, making the constraints brought by CO<sub>2</sub> or S profiles almost negligible. Another approach is to weight the  $NErr_j$  values either with analytical uncertainty [Myers et al., 2018] or maximum measured concentration in the embayment [Newcombe et al., 2020] of volatile species. Weighting the concentration with the error value nondimensionalizes the profile and gives equal weight to the quality of fit of each volatile specie. In EMBER, the  $NErr_j$  values are weighted by the analytical uncertainty on each volatile concentration. It results in an even consideration of the constraints brought by each volatile species. There are pros and cons for this choice, if one thinks the S degassing model to not be as accurate as the H<sub>2</sub>O degassing model for instance, one may choose not to weigh and scale the errors. The user ultimately must make the choice and it should be reported.

## 5. Recalculation of decompression rates

In the previous section, we presented EMBER calculation results using initial conditions ( $C_i$ ,  $M_0$  if studied, range of dPdt,  $P_{end}$ ,  $P_{start}$ ) directly from the original literature studies to demonstrate the quality of EMBER and its ability to reproduce the former literature results. Now, we use EMBER to reprocess the raw data from the literatures, but this time using a uniform protocol that takes into account the following parameters: the presence of exsolved gas, the same set of formulas for diffusion coefficient calculation, a model with a single step ascent and an initial volatile element concentration, determined from the concentration plateau (Table 2). Detailed modelled profiles of each embayments can be found in the supplementary materials. We restricted the calculations to 3 profiles per eruption for Myers et

al., [2018], including the ones associated with the highest and lowest decompression rate recorded, and to 5 profiles for Myers et al., [2021].

## 5.1 The impact of calculation strategies

Our hope with developing EMBER is to minimize differences in modelling parameters (e.g., diffusion coefficients, error treatment, minimization strategy...) in future studies. It is important to realize however that differences in strategies will persist. For instance, whilst EMBER allow the user to set the exsolved gas content ( $M_0$ ) as a free parameter to be determined by a grid-search, some users might prefer to impose an exsolved gas content based on independent constraint. This is the case for instance of the Moussallam et al., [2019] study of the 2017-2018 Ambae eruption where, in a second set of calculations, the authors used the difference between the volatile content of the melt inclusions and the starting volatile content of the embayments to estimate the likely amount of exsolved volatile in the system at the initiation of ascent.

Another strategy is to use the volatile content of melt inclusions as starting conditions for the diffusion model instead of the measured plateau values in the embayment interior. This was the strategy adopted by Myers et al., [2021] for the Minoan eruption of Santorini, where a fixed initial concentration of 5.2 wt. %  $H_2O$  (except for one embayment at 5.6 wt. %  $H_2O$ ) was used for all model calculations. Such strategy was also used by Humphreys et al., [2008] for Mt St Helens calculations.

In this study, we recalculated all embayment profiles using the same strategy throughout, but we do not pass judgement on the validity of one strategy over another. Our aim is to present a dataset which is as comparable as possible. The data presented in Fig. 7 and Table 2 are hence all calculated leaving the exsolved volatile content ( $M_0$ ) as unconstrained (i.e., as a part of the

grid search) and using the plateau values in volatile content recorded in embayment interiors as the model starting conditions ( $C_i$ ).

This difference in starting assumptions can lead to significant differences in the resulting decompression rate. Recalculating the embayment data from Myers et al., [2021] with our protocol leads to decompression rates 3 to 20 times higher. It is therefore of paramount importance that users of EMBER explicitly report their assumptions and starting conditions. We recommend that future compilations continue to reprocess original data in a consistent manner (as done here) in order to render inter-study comparison as coherent as possible.

## 5.2 Decompression rates vs eruption parameters

A recent literature compilation showed a clear relationship between magma decompression rate and whether an eruption is explosive or effusive in character [Cassidy et al., 2018]. This relationship deserves more scrutiny to establish if finer relationships between magma decompression rates and explosivity exists in nature. The VEI (Volcanic Explosivity Index), as an approximation of eruption explosivity, is related to eruption magnitude and/or plume height [Newhall and Self., 1982]. To show the utility of EMBER for the studies of volcanic explosivity, we tested the presence (or absence) of a correlation between decompression rate and both eruption magnitude and plume height, with our reprocessed data. Previous studies have found that the eruption magnitude is positively correlated with decompression rate [Ferguson et al., 2016; Moussallam et al., 2019]. However, our compilation shows no clear correlation between decompression rate and eruption magnitude (Fig. 7a).

We notice that an increase in decompression rate with eruption magnitude is noticeable for basaltic magmas (Kīlauea, Ambae and Ambrym) but the correlation is weakly significant (Pearson coefficient of 0.24 with a p-value of 0.35 and  $R^2=0.47$ , which corresponds to a weak

positive correlation). In a single eruption, there can be varying flow regime creating a range of decompression rate within the conduit; a batch of magma potentially ascend faster than the others (e.g., [Martel et al., 1998; Gonnermann and Manga., 2007; Cassidy et al., 2015]). If we only consider the highest decompression rate of any given eruption however, the aforementioned weak correlation between decompression rate and magnitude becomes more significant for mafic eruptions (Figure 7a) (Pearson coefficient of 0.93 with a p-value of 0.01 and  $R^2=0.86$ ). The calculated decompression rates for rhyolitic eruptions on the other hand shows no correlation with eruption magnitude.

The eruption intensity is also assessed with the plume height, which is directly observed or calculated through several empirically-determined relations involving isopachs for explosive eruptions (e.g., [Woods and Wohletz., 1991; Mastin et al., 2009; Pyle., 2015]). The eruption intensity, estimated from the mass eruption rate, has been shown to be positively correlated with decompression rate [Barth et al., 2019; Ferguson et al., 2016; Newcombe et al., 2020]. Thus, the plume height is expected to correlate with the decompression rate. We used EMBER-recalculated decompression rates to test this hypothesis. For the two eruptions of Kīlauea for which the plume height is not constrained, we used the maximal height of the lava fountain instead. Ambrym's plume height data for the 2018 eruption is undetermined and therefore not added to Figure 7b. Results show no global correlation between these two parameters (Figure 7b). However, considering again the highest decompression rate recorded for each eruption, a strong positive correlation emerges for basaltic eruptions (with a Pearson coefficient of 0.76, a p-value of 0.005 and  $R^2=0.88$ ). Again, the calculated decompression rate for rhyolitic eruptions shows no correlation with eruption plume height. The maximum decompression rate for basaltic eruption therefore shows a statistically significant positive correlation with both eruption magnitude and plume height. A first order positive correlation

therefore exists between the maximal magma decompression rate and the explosivity of an eruption for basaltic eruptions.

## 6. Conclusion

- We present EMBER, a user-friendly GUI program that calculates decompression rates from H<sub>2</sub>O, CO<sub>2</sub> and S concentration profiles along embayments of basaltic to rhyolitic compositions.
- We found that decompression rate calculations are particularly sensitive to variations of M<sub>0</sub> especially for the H<sub>2</sub>O diffusion profile. Variations of P<sub>end</sub> are also accompanied by a variation of the best fit exsolved gas content, but not necessarily by a variation of associated decompression rate.
- We recalculated decompression rates from previous studies twice: first, to validate and test how well EMBER reproduced existing results using the parameters from the original studies, and secondly, to homogenize determined decompression rates applying the same protocol to the existing raw data from previous studies, in order to improve inter-study comparison.
- In the first case, recalculated decompression rates are in the same order of magnitude as original calculations but notable differences do occur such as for the 1980 Mt St Helens eruption which recalculated decompression rate are at 0.15-0.41 MPa/s, half of the previously reported values [Humphreys et al., 2008].
- In the second case, recalculated dataset shows no significant correlation between magma decompression rate and eruption magnitude when considering the entire dataset and shows a weak correlation when considering the subset of decompression rates of basaltic magma (Pearson coefficient of 0.24 with a p-value of 0.35 and

R<sup>2</sup>=0.47.) The correlation is significant when considering only the maximum decompression rates of each basaltic eruption (Pearson coefficient of 0.93 with a p-value of 0.01 and R<sup>2</sup>=0.86). Additionally, there is no significant correlation between decompression rate and plume height when considering the entire dataset. However, once again, a statistically significant trend appears when considering only the maximum decompression rate of the basaltic eruptions (with a Pearson coefficient of 0.84, a p-value of 0.007 and R<sup>2</sup>=0.88).

- Our results suggest for the first time, a significant positive correlation, between embayment-calculated maximum decompression rate and eruption explosivity parameters such as magnitude and plume height, for basaltic eruptions.

## 7. Computer code availability

- Title of the software: EMBER
- Developers: Guillaume Georgeais, Kenneth T. Koga, Yves Moussallam, Estelle F. Rose-Koga
- Hardware used: EMBER was run on a computer with 4 core (4.5GHz) and 16GB of RAM
- Link to the software, tutorial and test using data from [Ferguson et al., 2016]  
DOI: [10.6084/m9.figshare.13663811](https://doi.org/10.6084/m9.figshare.13663811)
- Software required: MATLAB Runtime Environment 2019b and up  
<https://www.mathworks.com/products/compiler/matlab-runtime.html>

## Acknowledgement

We would like to thank M. Humphreys for providing the raw data of the Mt St Helens embayments. GG was supported by a PhD fellowship from the French Government “Ministère de l’Enseignement Supérieur, de la Recherche et de l’Innovation”. ERK acknowledges partial funding from Laboratory of Excellence initiative n°ANR-10-LABX-0006, the Région Auvergne and the European Regional Development Funds. Y.M acknowledges funding from INSU and the Région Auvergne Rhone Alpes. This is Laboratory of Excellence ClerVolc contribution number 463. We thank Madison Myers for sharing her code during the review process of our manuscript. We would like to thank Madison Myers and an Anonymous reviewer for their comments on the original manuscript and Marie Edmonds for editorial handling.

## Bibliography

- Aki, K., & Koyanagi, R. (1981). Deep volcanic tremor and magma ascent mechanism under Kilauea, Hawaii. *Journal of Geophysical Research*, 86(B8), 7095.  
<https://doi.org/10.1029/JB086iB08p07095>

584 Anderson, A. T. (1991). Hourglass inclusions: Theory and application to the Bishop Rhyolitic Tuff.  
 585 *American Mineralogist*, 76(3–4), 530–547.

586 Barth, A., Newcombe, M., Plank, T., Gonnermann, H., Hajimirza, S., Soto, G. J., et al. (2019). Magma  
 587 decompression rate correlates with explosivity at basaltic volcanoes — Constraints from  
 588 water diffusion in olivine. *Journal of Volcanology and Geothermal Research*, 387, 106664.  
 589 <https://doi.org/10.1016/j.jvolgeores.2019.106664>

590 Behrens, H., & Zhang, Y. (2001). Ar diffusion in hydrous silicic melts: Implications for volatile diffusion  
 591 mechanisms and fractionation. *Earth and Planetary Science Letters*, 192, 363–376.  
 592 [https://doi.org/10.1016/S0012-821X\(01\)00458-7](https://doi.org/10.1016/S0012-821X(01)00458-7)

593 Browne, B., & Gardner, J. (2006). The influence of magma ascent path on the texture, mineralogy,  
 594 and formation of hornblende reaction rims. *Earth and Planetary Science Letters*, 246(3–4),  
 595 161–176. <https://doi.org/10.1016/j.epsl.2006.05.006>

596 Carey, S., & Sigurdsson, H. (1985). The May 18, 1980 eruption of Mount St. Helens: 2. Modeling of  
 597 dynamics of the Plinian Phase. *Journal of Geophysical Research: Solid Earth*, 90(B4), 2948–  
 598 2958. <https://doi.org/10.1029/JB090iB04p02948>

599 Cassidy, M., Cole, Paul. D., Hicks, K. E., Varley, N. R., Peters, N., & Lerner, A. H. (2015). Rapid and  
 600 slow: Varying magma ascent rates as a mechanism for Vulcanian explosions. *Earth and*  
 601 *Planetary Science Letters*, 420, 73–84. <https://doi.org/10.1016/j.epsl.2015.03.025>

602 Cassidy, M., Manga, M., Cashman, K., & Bachmann, O. (2018). Controls on explosive-effusive volcanic  
 603 eruption styles. *Nature Communications*, 9(1), 2839. [https://doi.org/10.1038/s41467-018-](https://doi.org/10.1038/s41467-018-05293-3)  
 604 [05293-3](https://doi.org/10.1038/s41467-018-05293-3)

605 deGraffenried, R., & Shea, T. (2020). Modeling diffusion in 1D within melt embayments: correcting  
 606 for 3D geometry. Presented at the AGU Fall Meeting 2020, AGU. Retrieved from  
 607 <https://agu.confex.com/agu/fm20/meetingapp.cgi/Paper/676363>

608 Demouchy, S., & Mackwell, S. (2006). Mechanisms of hydrogen incorporation and diffusion in iron-  
609 bearing olivine. *Physics and Chemistry of Minerals*, 33(5), 347–355.  
610 <https://doi.org/10.1007/s00269-006-0081-2>

611 Faure, F., & Schiano, P. (2005). Experimental investigation of equilibration conditions during  
612 forsterite growth and melt inclusion formation. *Earth and Planetary Science Letters*, 236(3),  
613 882–898. <https://doi.org/10.1016/j.epsl.2005.04.050>

614 Ferguson, D. J., Gonnermann, H. M., Ruprecht, P., Plank, T., Hauri, E. H., Houghton, B. F., & Swanson,  
615 D. A. (2016). Magma decompression rates during explosive eruptions of Kīlauea volcano,  
616 Hawaii, recorded by melt embayments. *Bulletin of Volcanology*, 78(10), 71.  
617 <https://doi.org/10.1007/s00445-016-1064-x>

618 Freda, C., Baker, D. R., Romano, C., & Scarlato, P. (2003). Water diffusion in natural potassic melts.  
619 *Geological Society, London, Special Publications*, 213(1), 53–62.  
620 <https://doi.org/10.1144/GSL.SP.2003.213.01.04>

621 Freda, Carmela, Baker, D. R., & Scarlato, P. (2005). Sulfur diffusion in basaltic melts. *Geochimica et*  
622 *Cosmochimica Acta*, 69(21), 5061–5069. <https://doi.org/10.1016/j.gca.2005.02.002>

623 Gardner, J. E., Sigurdsson, H., & Carey, S. N. (1991). Eruption dynamics and magma withdrawal during  
624 the Plinian Phase of the Bishop Tuff Eruption, Long Valley Caldera. *Journal of Geophysical*  
625 *Research*, 96(B5), 8097. <https://doi.org/10.1029/91JB00257>

626 Geschwind, C.-H., & Rutherford, M. J. (1995). Crystallization of microlites during magma ascent: the  
627 fluid mechanics of 1980–1986 eruptions at Mount St Helens. *Bulletin of Volcanology*, 57(5),  
628 356–370. <https://doi.org/10.1007/BF00301293>

629 Girona, T., & Costa, F. (2013). DIPRA: A user-friendly program to model multi-element diffusion in  
630 olivine with applications to timescales of magmatic processes. *Geochemistry, Geophysics,*  
631 *Geosystems*, 14(2), 422–431. <https://doi.org/10.1029/2012GC004427>

632 Gonnermann, H. M., & Manga, M. (2007). The Fluid Mechanics Inside a Volcano. *Annual Review of*  
633 *Fluid Mechanics*, 39(1), 321–356. <https://doi.org/10.1146/annurev.fluid.39.050905.110207>

634 Humphreys, M. C. S., Menand, T., Blundy, J. D., & Klimm, K. (2008a). Magma ascent rates in explosive  
 635 eruptions: Constraints from H<sub>2</sub>O diffusion in melt inclusions. *Earth and Planetary Science*  
 636 *Letters*, 270(1–2), 25–40. <https://doi.org/10.1016/j.epsl.2008.02.041>  
 637 Humphreys, M. C. S., Menand, T., Blundy, J. D., & Klimm, K. (2008b). Magma ascent rates in explosive  
 638 eruptions: Constraints from H<sub>2</sub>O diffusion in melt inclusions. *Earth and Planetary Science*  
 639 *Letters*, 270(1–2), 25–40. <https://doi.org/10.1016/j.epsl.2008.02.041>  
 640 Johnston, E., R.S.J., S., Phillips, J., & Carey, S. (2014). Revised Estimates for the Volume of the Late  
 641 Bronze Age Minoan Eruption, Santorini, Greece. *Journal of the Geological Society*, 171.  
 642 <https://doi.org/10.1144/jgs2013-113>  
 643 Klein, F. W., Koyanagi, R. Y., Nakata, J. S., & Tanigawa, W. R. (1987). The seismicity of Kilauea's  
 644 magma system. *US Geol. Surv. Prof. Pap.*, 1350(2), 1019–1185.  
 645 Klügel, A. (1998). Reactions between mantle xenoliths and host magma beneath La Palma (Canary  
 646 Islands): constraints on magma ascent rates and crustal reservoirs. *Contributions to*  
 647 *Mineralogy and Petrology*, 131(2), 237–257. <https://doi.org/10.1007/s004100050391>  
 648 Klügel, A., Hansteen, T. H., & Schmincke, H.-U. (1997). Rates of magma ascent and depths of magma  
 649 reservoirs beneath La Palma (Canary Islands). *Terra Nova*, 9(3), 117–121.  
 650 <https://doi.org/10.1046/j.1365-3121.1997.d01-15.x>  
 651 Kohlstedt, D. L., & Mackwell, S. J. (1998). Diffusion of hydrogen and intrinsic point defects in olivine.  
 652 *Zeitschrift Fur Physikalische Chemie*, 207(1–2), 147–162.  
 653 Le Voyer, M., Asimow, P. D., Mosenfelder, J. L., Guan, Y., Wallace, P. J., Schiano, P., et al. (2014).  
 654 Zonation of H<sub>2</sub>O and F Concentrations around Melt Inclusions in Olivines. *Journal of*  
 655 *Petrology*, 55(4), 685–707. <https://doi.org/10.1093/petrology/egu003>  
 656 Liu, Y., Anderson, A. T., & Wilson, C. J. N. (2007). Melt pockets in phenocrysts and decompression  
 657 rates of silicic magmas before fragmentation. *Journal of Geophysical Research*, 112(B6),  
 658 B06204. <https://doi.org/10.1029/2006JB004500>

659 Lloyd, A. S., Ruprecht, P., Hauri, E. H., Rose, W., Gonnermann, H. M., & Plank, T. (2014). NanoSIMS  
 660 results from olivine-hosted melt embayments: Magma ascent rate during explosive basaltic  
 661 eruptions. *Journal of Volcanology and Geothermal Research*, 283, 1–18.  
 662 <https://doi.org/10.1016/j.jvolgeores.2014.06.002>

663 Mackwell, S. J., & Kohlstedt, D. L. (1990). Diffusion of hydrogen in olivine: Implications for water in  
 664 the mantle. *Journal of Geophysical Research*, 95(B4), 5079.  
 665 <https://doi.org/10.1029/JB095iB04p05079>

666 Martel, C., Pichavant, M., Bourdier, J.-L., Traineau, H., Holtz, F., & Scaillet, B. (1998). Magma storage  
 667 conditions and control of eruption regime in silicic volcanoes: experimental evidence from  
 668 Mt. Pelée. *Earth and Planetary Science Letters*, 156(1), 89–99.  
 669 [https://doi.org/10.1016/S0012-821X\(98\)00003-X](https://doi.org/10.1016/S0012-821X(98)00003-X)

670 Martel, Caroline, & Iacono-Marziano, G. (2015). Timescales of bubble coalescence, outgassing, and  
 671 foam collapse in decompressed rhyolitic melts. *Earth and Planetary Science Letters*, 412,  
 672 173–185. <https://doi.org/10.1016/j.epsl.2014.12.010>

673 Mason, B. G., Pyle, D. M., & Oppenheimer, C. (2004). The size and frequency of the largest explosive  
 674 eruptions on Earth. *Bulletin of Volcanology*, 66(8), 735–748. [https://doi.org/10.1007/s00445-](https://doi.org/10.1007/s00445-004-0355-9)  
 675 004-0355-9

676 Mastin, L., Van Eaton, A., & Lowenstern, J. (2014). Modeling ash fall distribution from a Yellowstone  
 677 supereruption. *Geochemistry, Geophysics, Geosystems*, 15.  
 678 <https://doi.org/10.1002/2014GC005469>

679 Mastin, L. G., Guffanti, M., Servranckx, R., Webley, P., Barsotti, S., Dean, K., et al. (2009). A  
 680 multidisciplinary effort to assign realistic source parameters to models of volcanic ash-cloud  
 681 transport and dispersion during eruptions. *Journal of Volcanology and Geothermal Research*,  
 682 186(1), 10–21. <https://doi.org/10.1016/j.jvolgeores.2009.01.008>

683 Moussallam, Y., Rose-Koga, E. F., Koga, K. T., Médard, E., Bani, P., Devidal, J.-L., & Tari, D. (2019). Fast  
 684 ascent rate during the 2017–2018 Plinian eruption of Ambae (Aoba) volcano: a petrological

685 investigation. *Contributions to Mineralogy and Petrology*, 174(11), 90.  
686 <https://doi.org/10.1007/s00410-019-1625-z>

687 Moussallam, Y., Médard, E., Georgeais, G., Rose-Koga, E. F., Koga, K. T., Pelletier, B., et al. (2021).  
688 How to turn off a lava lake? A petrological investigation of the 2018 intra-caldera and  
689 submarine eruptions of Ambrym volcano. *Bulletin of Volcanology*.  
690 <https://doi.org/10.1007/s00445-021-01455-2>

691 Myers, M. L., Wallace, P. J., Wilson, C. J. N., Watkins, J. M., & Liu, Y. (2018). Ascent rates of rhyolitic  
692 magma at the onset of three caldera-forming eruptions. *American Mineralogist*, 103(6), 952–  
693 965. <https://doi.org/10.2138/am-2018-6225>

694 Myers, M. L., Druitt, T. H., Schiavi, F., Gurioli, L., & Flaherty, T. (2021). Evolution of magma  
695 decompression and discharge during a Plinian event (Late Bronze-Age eruption, Santorini)  
696 from multiple eruption-intensity proxies. *Bulletin of Volcanology*, 83(3), 18.  
697 <https://doi.org/10.1007/s00445-021-01438-3>

698 Newcombe, M. E., Plank, T., Barth, A., Asimow, P. D., & Hauri, E. (2020). Water-in-olivine magma  
699 ascent chronometry: Every crystal is a clock. *Journal of Volcanology and Geothermal*  
700 *Research*, 398, 106872. <https://doi.org/10.1016/j.jvolgeores.2020.106872>

701 Newhall, C. G., & Self, S. (1982). The volcanic explosivity index (VEI) an estimate of explosive  
702 magnitude for historical volcanism. *Journal of Geophysical Research*, 87(C2), 1231.  
703 <https://doi.org/10.1029/JC087iC02p01231>

704 Newman, S., & Lowenstern, J. B. (2002). VolatileCalc: a silicate melt–H<sub>2</sub>O–CO<sub>2</sub> solution model  
705 written in Visual Basic for excel. *Computers & Geosciences*, 28(5), 597–604.  
706 [https://doi.org/10.1016/S0098-3004\(01\)00081-4](https://doi.org/10.1016/S0098-3004(01)00081-4)

707 Ni, H., & Zhang, L. (2018). A general model of water diffusivity in calc-alkaline silicate melts and  
708 glasses. *Chemical Geology*, 478, 60–68. <https://doi.org/10.1016/j.chemgeo.2017.10.010>

709 Nowak, M., & Behrens, H. (1997). An experimental investigation on diffusion of water in  
710 haplogranitic melts. *Contributions to Mineralogy and Petrology*, 126(4), 365–376.  
711 <https://doi.org/10.1007/s004100050256>

712 Nowak, Marcus, Schreen, D., & Spickenbom, K. (2004). Argon and CO<sub>2</sub> on the race track in silicate  
713 melts: A tool for the development of a CO<sub>2</sub> speciation and diffusion model. *Geochimica et*  
714 *Cosmochimica Acta*, 68, 5127–5138. <https://doi.org/10.1016/j.gca.2004.06.002>

715 Pyle, D. M. (2015). Sizes of Volcanic Eruptions. In *The Encyclopedia of Volcanoes* (pp. 257–264).  
716 Elsevier. <https://doi.org/10.1016/B978-0-12-385938-9.00013-4>

717 Rutherford, M. J. (2008). Magma Ascent Rates. *Reviews in Mineralogy and Geochemistry*, 69(1), 241–  
718 271. <https://doi.org/10.2138/rmg.2008.69.7>

719 Rutherford, Malcolm J., & Hill, P. M. (1993). Magma ascent rates from amphibole breakdown: An  
720 experimental study applied to the 1980–1986 Mount St. Helens eruptions. *Journal of*  
721 *Geophysical Research: Solid Earth*, 98(B11), 19667–19685.  
722 <https://doi.org/10.1029/93JB01613>

723 Scandone, R., & Malone, S. D. (1985). Magma supply, magma discharge and readjustment of the  
724 feeding system of mount St. Helens during 1980. *Journal of Volcanology and Geothermal*  
725 *Research*, 23(3–4), 239–262. [https://doi.org/10.1016/0377-0273\(85\)90036-8](https://doi.org/10.1016/0377-0273(85)90036-8)

726 Self, S. (2006). The effects and consequences of very large explosive volcanic eruptions. *Philosophical*  
727 *Transactions of the Royal Society A: Mathematical, Physical and Engineering Sciences*,  
728 364(1845), 2073–2097. <https://doi.org/10.1098/rsta.2006.1814>

729 Shreve, T., Grandin, R., Boichu, M., Garaebiti, E., Moussallam, Y., Ballu, V., et al. (2019). From  
730 prodigious volcanic degassing to caldera subsidence and quiescence at Ambrym (Vanuatu):  
731 the influence of regional tectonics. *Scientific Reports*, 9(1), 18868.  
732 <https://doi.org/10.1038/s41598-019-55141-7>

733 Sparks, R. S. J., Baker, L., Brown, R., Field, M., Schumacher, J., Stripp, G., & L. Walters, A. (2006).  
734 Dynamical constraints on kimberlite volcanism. *Journal of Volcanology and Geothermal*  
735 *Research*, 155, 18–48. <https://doi.org/10.1016/j.jvolgeores.2006.02.010>

736 Toramaru, A. (2006). BND (bubble number density) decompression rate meter for explosive volcanic  
737 eruptions. *Journal of Volcanology and Geothermal Research*, 154(3–4), 303–316.  
738 <https://doi.org/10.1016/j.jvolgeores.2006.03.027>

739 Toramaru, Atsushi. (1989). Vesiculation process and bubble size distributions in ascending magmas  
740 with constant velocities. *Journal of Geophysical Research*, 94(B12), 17523.  
741 <https://doi.org/10.1029/JB094iB12p17523>

742 Toramaru, Atsushi. (1995). Numerical study of nucleation and growth of bubbles in viscous magmas.  
743 *Journal of Geophysical Research: Solid Earth*, 100(B2), 1913–1931.  
744 <https://doi.org/10.1029/94JB02775>

745 Tryggvason, E. (1994). Surface deformation at the Krafla volcano, North Iceland, 1982–1992. *Bulletin*  
746 *of Volcanology*, 56(2), 98–107. <https://doi.org/10.1007/BF00304105>

747 Van Eaton, A., Herzog, M., Wilson, C., & McGregor, J. (2012). Ascent dynamics of large  
748 phreatomagmatic eruption clouds: The role of microphysics. *Journal of Geophysical Research*  
749 *(Solid Earth)*, 117, 3203. <https://doi.org/10.1029/2011JB008892>

750 Witham, F., Blundy, J., Kohn, S. C., Lesne, P., Dixon, J., Churakov, S. V., & Botcharnikov, R. (2012).  
751 SolEx: A model for mixed COHSCI-volatile solubilities and exsolved gas compositions in basalt.  
752 *Computers & Geosciences*, 45, 87–97. <https://doi.org/10.1016/j.cageo.2011.09.021>

753 Woods, A. W., & Wohletz, K. (1991). Dimensions and dynamics of co-ignimbrite eruption columns.  
754 *Nature*, 350(6315), 225–227. <https://doi.org/10.1038/350225a0>

755 Zhang, Y., & Behrens, H. (2000). H<sub>2</sub>O diffusion in rhyolitic melts and glasses. *Chemical Geology*,  
756 169(1), 243–262. [https://doi.org/10.1016/S0009-2541\(99\)00231-4](https://doi.org/10.1016/S0009-2541(99)00231-4)

757 Zhang, Y., Xu, Z., Zhu, M., & Wang, H. (2007). Silicate melt properties and volcanic eruptions: SILICATE  
758 MELT PROPERTIES. *Reviews of Geophysics*, 45(4). <https://doi.org/10.1029/2006RG000216>

759 Zhang, Y., Ni, H., & Chen, Y. (2010). Diffusion Data in Silicate Melts. *Reviews in Mineralogy and*  
760 *Geochemistry*, 72(1), 311–408. <https://doi.org/10.2138/rmg.2010.72.8>

761

762

## Figure caption

**Figure 1 :** Flow chart showing the calculation steps used in EMBER to determine the parameters and associated errors resulting in the best fit of natural volatile diffusion profiles. The outputs are a decompression rate and an initial (dissolved) volatile concentration as well as their associated confidence interval. This process of calculation is repeated for each value of exsolved volatile content ( $M_0$ ). Estimation of the  $M_0$  value and its related uncertainty is done in a similar manner but by considering the range of  $M_0$  variation as the 4<sup>th</sup> dimension of the starting matrix.

**Figure 2:** A display example of EMBER's GUI after a cycle of calculations. Input parameters are entered on the left panel (part 1) and results are displayed on the right (part 2). The input section is divided in three main parts, the grid search definition (1a), the main parameters and model selection (1b), and the parameters for the Monte-Carlo simulation (uncertainty and number of iterations) (1c). The result section is in three parts: comparison between best fit and natural diffusion profiles (2a), the result parameter of each best fit (2b) and the log section to follow the evolution of the calculation (2c). Clicking on the "Display all figures" once the program is done with the calculation will display best fits for each exsolved volatile content value and for each studied volatile specie. It also displays 3 3D-plots, of the evolution of the calculative error for each volatile(1) vs. the decompression rate and initial concentration, (2) the evolution of the decompression rate vs. exsolved volatile content and initial volatile concentration for each studied volatile specie and (3) the evolution of the cumulative error vs. decompression rate and exsolved volatile content (Figure 3 ).

**Figure 3:** Subset of plots generated from a calculation on the 1500CE Kīlauea reticulite ReaE1 studied previously by Ferguson et al., [2016]. (a) Influence of exsolved volatile content  $M_0$  on best fit diffusion profiles of  $H_2O$ . Initial parameters from the grid search are listed in the caption. (b) Best fit diffusion profiles calculated by considering  $H_2O$  only (solid line) or all studied species (dashed lines). (c) Evolution of the cumulated scaled  $\log_{10}$  (NErr\_m) values over a range of decompression rate and exsolved volatile content. (d) Evolution of the NErr\_m value for each volatile over a range of decompression rate and initial volatile content. The NErr\_m values are in a  $\log_{10}$  scale. The values of interest, linked to the smallest error value, are highlighted by a blue, red or yellow dot for  $H_2O$ ,  $CO_2$  and S respectively (d), and a black dot for the cumulative error (c).

**Figure 4 :** Comparison between recalculated data with EMBER and previous estimation from the literature. EMBER estimations are comparable with literature estimates with a few systematic differences (see text for details). Dashed line indicates the 1:1 ratio and thin solid lines indicates 2:1 and 0.5:1 ratios. Results from EMBER were acquired taking the input conditions of the respective original studies. Calculations for samples from Lloyd et al., :[2014] were made using their original  $H_2O$  diffusion coefficient. All the results displayed are

calculated for  $M_0=0$  excepted when original studies provided a range of  $M_0$  [Ferguson et al., 2016]. EMBER calculations were made using the “weighting and scaling of error” option which is a source of difference with previously reported literature decompression rate.

**Figure 5 :** Statistical repartition of all filtered decompression rate values with increasing iteration count of the Monte Carlo approach. The repartition gradually acquires a more pronounced shape. The red bars indicates the 1- $\sigma$  confidence interval of those decompression rates while the blue, green and black ones respectively indicate the best-fit result, the median and the mean. Calculation is done with fixed initial concentration and exsolved volatile content. All displayed data are in MPa/s

**Figure 6:** Evolution of modeled relative decompression rates from  $H_2O$  (a),  $CO_2$  (b) and S (c) as a function of the exsolved volatile content for a selection of embayments. Each case in a), b) or c) is calculated with a fixed  $P_{end}$ , reported in Table 2. For figures (d), (e) and (f),  $P_{ref}$  is the  $P_{end}$  value displayed in Table 2 for ReE2 and BT251. (d) The initial exsolved volatile content needed to generate the best fit ( $M_{Bestfit}$ ) increases for ReE2 when changing  $P_{end}$  but not systematically for M413. (e) Variation of relative decompression rate modeled from the  $H_2O$  diffusion profile only with  $P_{end}$ . (f) Variation of relative decompression rate modeled from all studied species ( $H_2O$ ,  $CO_2$  and S for ReE2, and  $H_2O$  and  $CO_2$  for M413) with  $P_{end}$ .

**Figure 7 :** (a) Compilation of EMBER-recalculated decompression rate as a function of eruption magnitude. The bigger mark indicates the highest decompression rate estimate for each eruption. For basaltic magmas, there is a trend of increasing decompression rate related to increasing magnitude only when considering the maximum decompression rate values. The trend does not apply to rhyolitic magmas. (b) Compilation of EMBER-recalculated decompression rate as a function of eruption plume height. The bigger mark indicates the highest decompression rate estimate for each eruption. With the exception of Ambrym, which plume maximal height is unknown and assessed by lava fountain height, there is a notable correlation between maximal decompression rate and plume height for basaltic magmas. The same caption applies for both figures. Magnitude estimates were calculated from either original article or respectively Shreve et al., [2019], Johnston et al., [2014], Self, [2006] and Mason et al., [2004] for Ambrym's 2018 eruption, Santorini's Minoan eruption, Taupo's Oruanui eruption and both Long Valley's Bishop Tuff and Yellowstone's Huckleberry Ridge Tuff. Plume height estimation comes from modelisations from Gardner et al., [1991], Mastin et al., [2014] and Van Eaton et al., [2012] respectively for Long Valley's Bishop Tuff, Yellowstone's Huckleberry Ridge Tuff and Taupo's Oruanui eruptions.

## Table caption

**Table 1 :** Comparison of previously published codes. EMBER is a fully available complete software that covers a large spectrum of magma composition:  $dPdt$  = decompression rate,  $C_i$  = initial concentration,  $M_0$  = exsolved volatile content,  $P_f$  = pressure of quench, gs stands for “grid search”. Every study that model decompression rates from  $CO_2$  and/or S uses the diffusion coefficients calculated from [Zhang et al., 2007]. The only two exceptions are the  $CO_2$  diffusivity from [Liu et al.,

846 2007] which is calculated from [Behrens and Zhang, 2001] and the S diffusivity from [Ferguson et al.,  
847 2016], which is calculated from [Freda et al., 2005].

848

849

850 **Table 2** : Re-calculated decompression rates with initial conditions and related eruption parameters.  
851 Ascent rates were calculated with density values from each original studies using the equation  
852  $Asc\_rate = (Decomp\_rate / 9.81 * Crustal\_density) * 10^6$  with *Decomp\_rate* in MPa/s, *Asc\_rate*  
853 in m/s and the crustal density in kg/m<sup>3</sup>

854

855

856

857 **Tables**

858 **Table 1**

Article	Architecture	Volatiles studied	Magmatic composition	H <sub>2</sub> O diffusion coefficient	Input parameters	M <sub>0</sub> study	Availability
Liu et al, 2007	FORTRAN 77	H <sub>2</sub> O	Rhyolitic	a	dPdt, C <sub>i</sub> , T, M <sub>0</sub> , P <sub>f</sub> , P <sub>0</sub> *	yes	On request
Humphreys et al, 2008	COMSOL	H <sub>2</sub> O	Rhyolitic	a ; b	dPdt, C <sub>i</sub> P <sub>f</sub> , P <sub>0</sub> , T *		
Lloyd et al, 2014	n.d	H <sub>2</sub> O,CO <sub>2</sub> ,S	Intermediate	Self-determined empiric law	dPdt, P <sub>f</sub> , P <sub>0</sub> , C <sub>i</sub> , T *		
Ferguson et al, 2016	MATLAB	H <sub>2</sub> O,CO <sub>2</sub> ,S	Basaltic	c	gs(dPdt, C <sub>i</sub> , M <sub>0</sub> ), P <sub>f</sub> , P <sub>0</sub> , T	yes	
Myers et al, 2018	MATLAB	H <sub>2</sub> O,CO <sub>2</sub>	Rhyolitic	a	gs(dPdt, P <sub>f</sub> , M <sub>0</sub> ), C <sub>i</sub> , P <sub>0</sub> , T	yes	On request
Moussallam et al, 2019	RStudio	H <sub>2</sub> O	Basaltic	Constant ( e )	dPdt, C <sub>i</sub> , P <sub>f</sub> , P <sub>0</sub> , T	yes	Publicly Available
Newcombe et al, 2020	MATLAB	H <sub>2</sub> O,CO <sub>2</sub> ,S	Intermediate	d	dPdt, M <sub>0</sub> , P <sub>f</sub> , P <sub>0</sub> , T *	yes	
EMBER (This study)	MATLAB	H <sub>2</sub> O,CO <sub>2</sub> ,S	Basaltic, Intermediate and Rhyolitic	e ; d ; a	gs(dPdt, C <sub>i</sub> , M <sub>0</sub> ), P <sub>f</sub> , P <sub>0</sub> , T	yes	Publicly Available

a = [Zhang and Behrens, 2000]  
b = [Nowak and Behrens, 1997]

c = [Zhang et al., 2010]  
d = [Ni and Zhang, 2018]

e = [Freda et al., 2003]  
\*unconfirmed use of a grid search

859

860

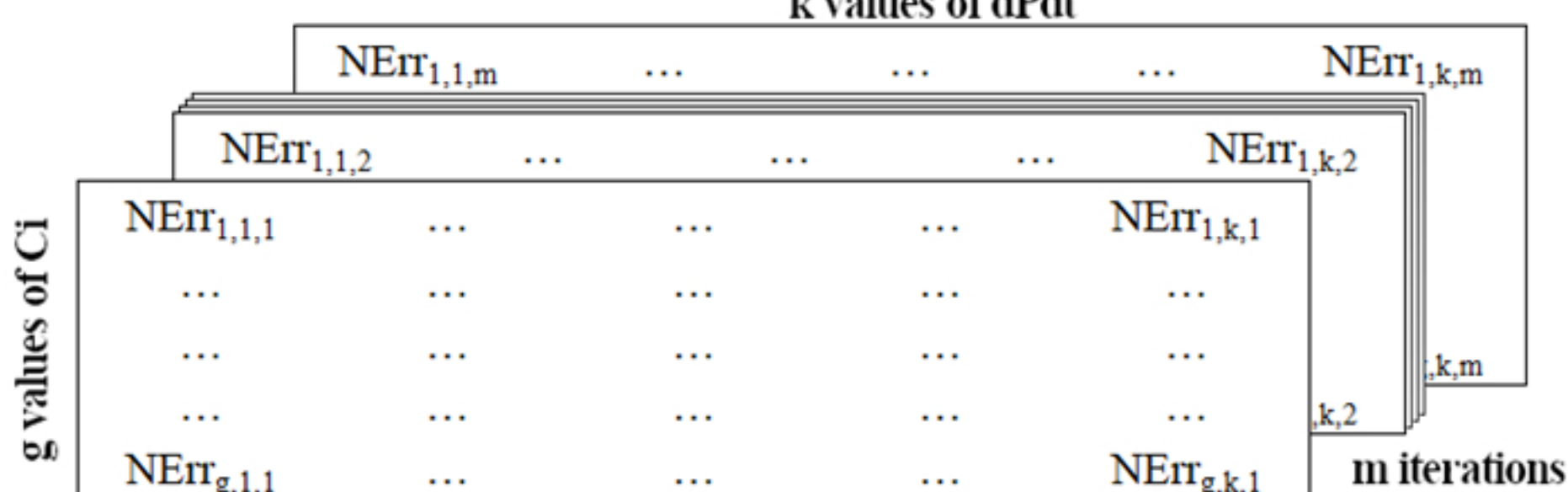
861     **Table 2**

862

	Decompression rate (Mpa/s)				Ascent rate (m/s)	Initial concentration			M (wt%)	Time of ascension (s)	Pstart (MPa)	Pend (MPa)	T(°C)	Magnitude
	H2O based	CO2 based	S based	all species		H2O (wt%)	CO2 (ppm)	S (ppm)						
Ferguson et al., 2016														
IkiE1	0.03 + 0.01 - 0.00	0.02 + 0.00 - 0.00	0.04 + 0.01 - 0.00	0.04 + 0.00 - 0.00	1.4	0.60 + 0.00 - 0.00	300 + 0 - 0	1390 + 0 - 0	0.1 + 0.1 - 0.0	2755	107	0.1	1192	1.5
ReticE1	0.08 + 0.03 - 0.01	0.09 + 0.02 - 0.01	0.08 + 0.04 - 0.02	0.08 + 0.02 - 0.01	2.9	0.55 + 0.00 - 0.00	184 + 0 - 0	1316 + 0 - 0	1.6 + 0.0 - 0.0	553	47	2.75	1163	2.5
ReticE2	0.07 + 0.03 - 0.01	0.03 + 0.01 - 0.00	0.40 + 0.00 - 0.03	0.06 + 0.02 - 0.00	2.1	0.57 + 0.00 - 0.00	170 + 0 - 0	1320 + 0 - 0	3.2 + 0.0 - 0.0	676	40	0.1	1163	2.5
KeaE1	0.28 + 0.10 - 0.05	0.11 + 0.04 - 0.01	0.35 + 0.25 - 0.16	0.26 + 0.05 - 0.04	9.3	0.52 + 0.03 - 0.00	265 + 5 - 0	1415 + 5 - 0	1.6 + 0.8 - 0.0	185	50	2	1160	2.6
Moussallam et al., 2019														
AO2	0.46 + 0.27 - 0.18				16.0	1.32 + 0.00 - 0.00			0.1 + 0.1 - 0.0	110	50	0.1	1150	3.3
AO13	0.12 + 0.03 - 0.01				4.2	1.15 + 0.00 - 0.00			1.6 + 1.6 - 1.4	253	30	0.1	1150	3.3
AO38	0.17 + 0.05 - 0.03		0.39 + 0.01 - 0.16	0.19 + 0.08 - 0.07	6.7	1.15 + 0.00 - 0.00		403 + 0 - 0	0.8 + 0.5 - 0.0	237	45	0.1	1150	3.3
Lloyd et al., 2014														
E1	0.24 + 0.01 - 0.04	0.03 + 0.00 - 0.00	0.01 + 0.00 - 0.00	0.06 + 0.03 - 0.02	2.2	4.00 + 0.00 - 0.00	100 + 0 - 0	1500 + 0 - 0	0.1 + 0.3 - 0.1	3333	202	2	1030	4.4
E2	1.07 + 0.29 - 0.26	0.10 + 0.00 - 0.00	0.13 + 0.34 - 0.03	0.30 + 0.03 - 0.09	11.1	2.20 + 0.10 - 0.00	150 + 3 - 0	1900 + 33 - 0	0 + 0.2 - 0.0	175	54.6	2	1030	4.4
E3	0.92 + 0.47 - 0.21	1.47 + 0.03 - 0.59		1.10 + 0.32 - 0.29	40.9	2.80 + 0.00 - 0.00	160 + 0 - 0		1.6 + 1.6 - 1.2	69	78	2	1030	4.4
E4	0.35 + 0.08 - 0.05	0.28 + 0.13 - 0.08	0.46 + 0.01 - 0.27	0.44 + 0.01 - 0.10	16.3	2.80 + 0.00 - 0.00	170 + 0 - 0	2070 + 0 - 0	0.1 + 0.1 - 0.0	498	221	2	1030	4.4
Myers et al., 2018														
BTF7-1_RE_no_2	0.021 + 0.002 - 0.003				0.8	3.70 + 0.10 - 0.05			0.4 + 2.8 - 0.2	3238	78	10	740	8.5
BT_F2-5_RE_no_1	0.041 + 0.011 - 0.010				1.6	3.80 + 0.00 - 0.00			1.6 + 1.6 - 1.4	1014	77	35	740	8.5
BTF8-2_RE_no_1	0.273 + 0.061 - 0.061				10.7	5.00 + 0.00 - 0.00			0.1 + 1.5 - 0.1	264	131	59	740	8.5
P1963-6_RE_no_1	0.007 + 0.002 - 0.002	0.0001 + 0.0004 - 0.000		0.002 + 0.002 - 0.001	0.1	1.80 + 0.00 - 0.00	90 + 0 - 0		0 + 0.8 - 0.0	3846	38	13	780	8
P2305-F_RE_no_1	0.020 + 0.018 - 0.000				0.8	3.40 + 0.00 - 0.10			3.2 + 0.0 - 0.3	900	68	50	780	8
P1970-A_RE_no_6	0.068 + 0.058 - 0.035	0.010 + 0.004 - 0.000		0.033 + 0.072 - 0.019	1.3	3.40 + 0.10 - 0.00	90 + 10 - 0		0.1 + 0.7 - 0.1	515	89	54	780	8
MM4_RE_no_12	0.009 + 0.014 - 0.004	0.001 + 0.000 - 0.000		0.005 + 0.000 - 0.000	0.2	2.00 + 0.00 - 0.00	390 + 0 - 0		0 + 0.1 - 0.0	4934	85	40	800	9
MM7_RE_no_10	0.099 + 0.065 - 0.058	0.007 + 0.000 - 0.000		0.013 + 0.006 - 0.006	0.5	2.50 + 0.56 - 0.00	170 + 8 - 0		3.2 + 0.0 - 0.2	467	71	25	800	9
MM4_RE_no_13	0.069 + 0.045 - 0.018	0.152 + 0.086 - 0.080		0.105 + 0.081 - 0.047	4.1	2.80 + 0.00 - 0.00	290 + 0 - 0		1.6 + 1.6 - 1.4	1272	98	10	800	9
Humphreys et al., 2008														
KV518b-1	0.16 + 0.00 - 0.00				6.4	4.60 + 1.66 - 0.00			0	662	137	33	880	4.9
MSH1-3	0.23 + 0.00 - 0.00				9.3	6.50 + 0.00 - 0.52			0	481	137	27	880	4.9
MSH1-6	0.82 + 0.04 - 0.02				33.3	6.50 + 0.00 - 0.48			0	157	137	9	880	4.9
Moussallam et al. (2021)														
AF2	2.64 + 1.55 - 1.27		5.87 + 0.14 - 2.96	2.64 + 2.41 - 1.55	99.5	1.48 + 0.03 - 0.03		220 + 10 - 10	3.2 + 0.0 - 0.4	26	68	0.1	1110	4
AD5	0.49 + 0.12 - 0.08		0.14 + 0.96 - 0.04	0.53 + 0.19 - 0.14	19.9	1.05 + 0.05 - 0.10		950 + 50 - 100	0.1 + 0.3 - 0.1	64	34	0.1	1110	4
AE38	0.11 + 0.03 - 0.02		0.01 + 0.00 - 0.00	0.11 + 0.04 - 0.03	4.2	1.05 + 0.10 - 0.00		950 + 233 - 0	0 + 0.2 - 0.0	335	37	0.1	1110	4
PG11	1.70 + 0.87 - 0.59		0.10 + 0.06 - 0.00	1.70 + 0.86 - 0.59	64.1	1.80 + 0.20 - 0.10		797 + 33 - 17	1.6 + 1.6 - 1.4	68	115	0.1	1110	4
Myers et al, 2012														
18R1F	1.70 + 0.86 - 0.75				66.7	4.70 + 0.10 - 0.00		0	0	49	143	60	850	7.4
18R1O	1.70 + 0.56 - 0.40				66.7	4.30 + 0.08 - 0.00		0	0	55	119	26	850	7.4
18R2O	0.43 + 0.05 - 0.05				16.9	4.60 + 0.00 - 0.00		0	0	274	120	2	850	7.4
20R1O	0.47 + 0.01 - 0.08				18.4	3.35 + 0.05 - 0.03		0	0	153	77	5	850	7.4
11R6O	2.93 + 1.32 - 1.31				114.8	4.30 + 0.10 - 0.00		0	0	26	116	40	850	7.4

Figure 1.

**STEP 1**



- Mean for each  $NErr_{ij}$  values over the  $m$  iterations
- Select the minimal  $NErr\_m$  value
- Calculation of 1 sigma confidence interval over the  $NErr\_m_{a,b}$  value

**STEP 2**

$i=b$

$NErr\_m_{1,1}$	...	...	...	$NErr\_m_{1,k}$
...	...	...	...	...
...	...	$NErr\_m_{a,b}$	...	...
...	...	...	...	...
$NErr\_m_{g,1}$	...	...	...	$NErr\_m_{g,k}$

- Filtering of error values using equation 10

**STEP 3**

$i_1$   
 $i_2$   
 $i_3$

$NErr\_m_{1,1}$	$NErr\_m_{1,2}$	...	...	...	$NErr\_m_{1,k}$
$NErr\_m_{2,1}$	...	...	...	...	...
...	...	$NErr\_m_{i1,j1}$	...	...	...
...	...	...	...	$NErr\_m_{i2,j2}$	...
...	...	$NErr\_m_{i3,j1}$	...	...	...
$NErr\_m_{g,1}$	...	...	...	...	$NErr\_m_{g,k}$


- Extract the  $n$  values of  $dPdt$  and  $C_i$  that were used to calculate all the filtered  $NErr\_m_{ij}$

**STEP 4**

from all $j$	from all $i$
$dPdt_1$	$C_{i1}$
...	...
$dPdt_n$	$C_{in}$

**STEP 5**

- Result value of  $C_i$  and  $dPdt$
- 1 sigma confidence interval of  $C_i$  and  $dPdt$

 Smallest value among the whole matrix with (a,b) as its coordinates


 All  $NErr\_m_{ij}$  values that satisfy equation 10

Figure 2.

# Part 1: Inputs

# Part 2: Results

**Grid Search**

	Min	Max	Step
dPdt (MPa/s)	0.02	0.4	30
Cinit H2O (wt%)	0.57	0.63	4
Cinit CO2 (ppm)	170	192.5	
Cinit S (ppm)	1320	1330	
M value (wt%) (space separated): 0 0.1 0.2 0.4 0.8 1.6 3.2			

**General Inputs**

Temperature (°C) 1163

Pstart (MPa) 40

Pend (MPa) 2.75

File type: Magma Chemistry:

☒ Solex ☐ VolatileCalc

☒ CO2 study ☒ S study

Set working directory

**Uncertainty parameters**

H2O 2RSD (%)	6
CO2 2RSD (%)	4
S 2RSD (%)	2
Variability of spot place (μm)	2

Mole fraction of Si 0.5

Molar mass of anhydrous melt 35.5

Number of iterations 101

Name of the embayment ReE2

☒ Weighting and scaling of error

**Compute**

Calculation done

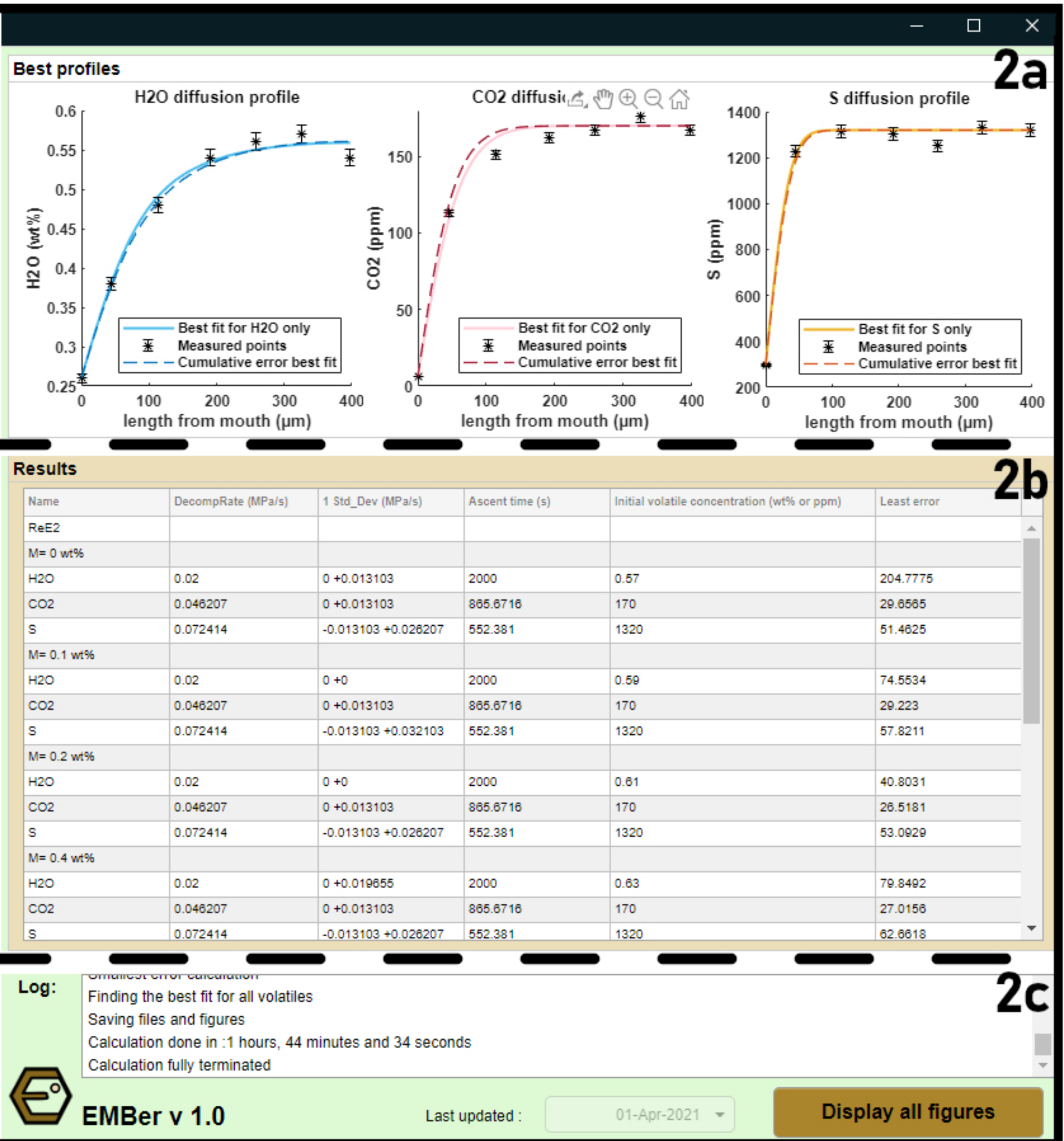
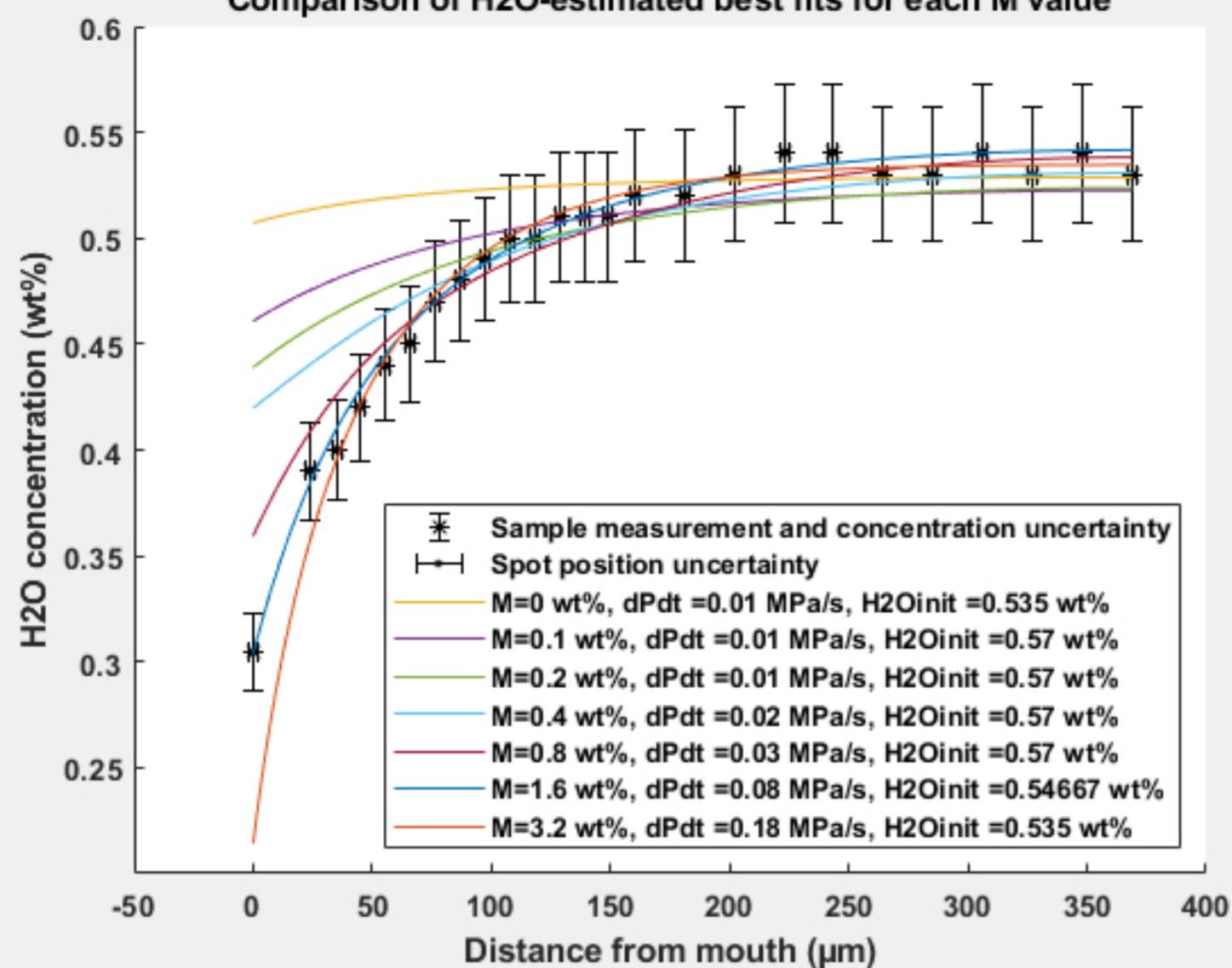
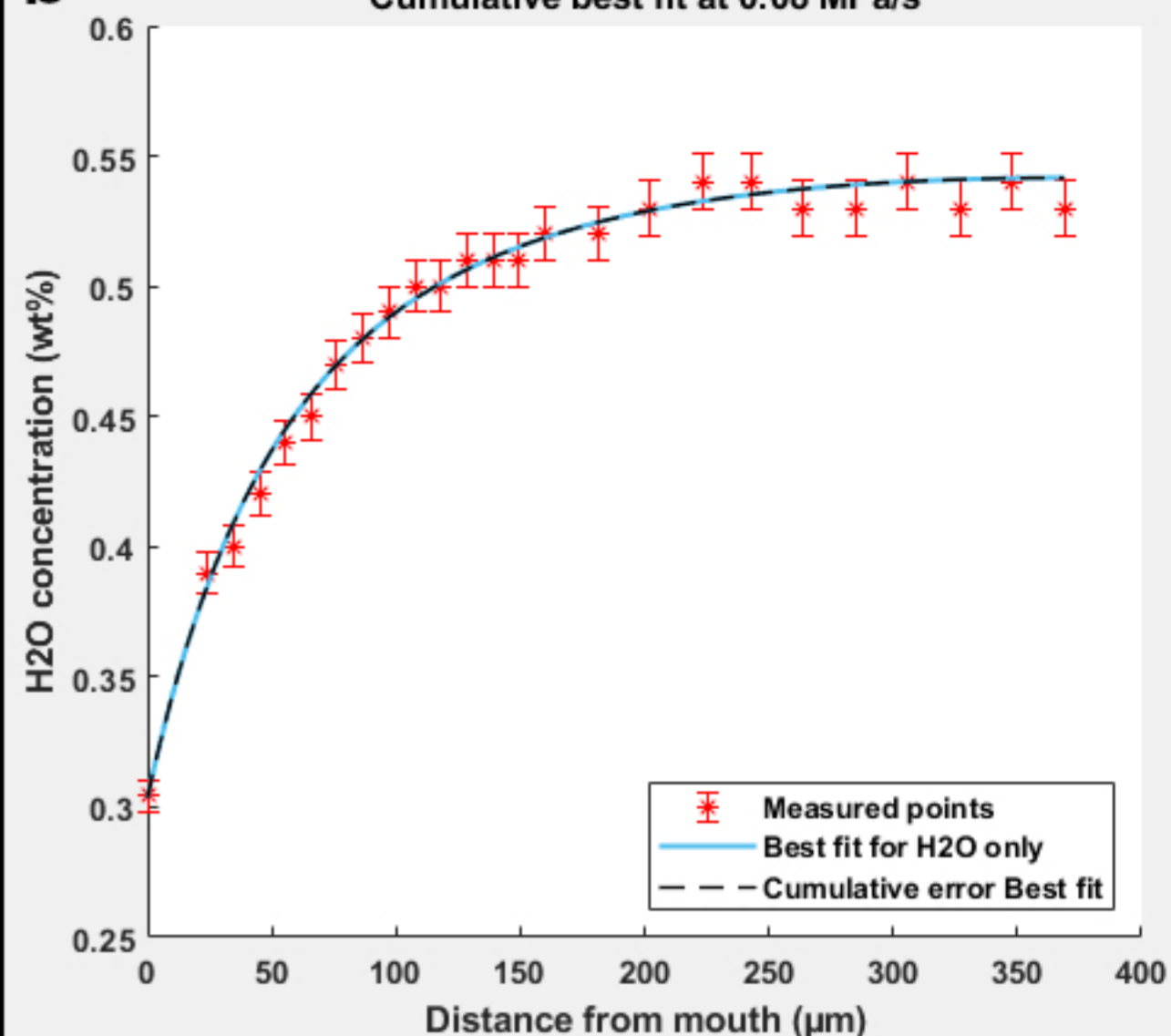


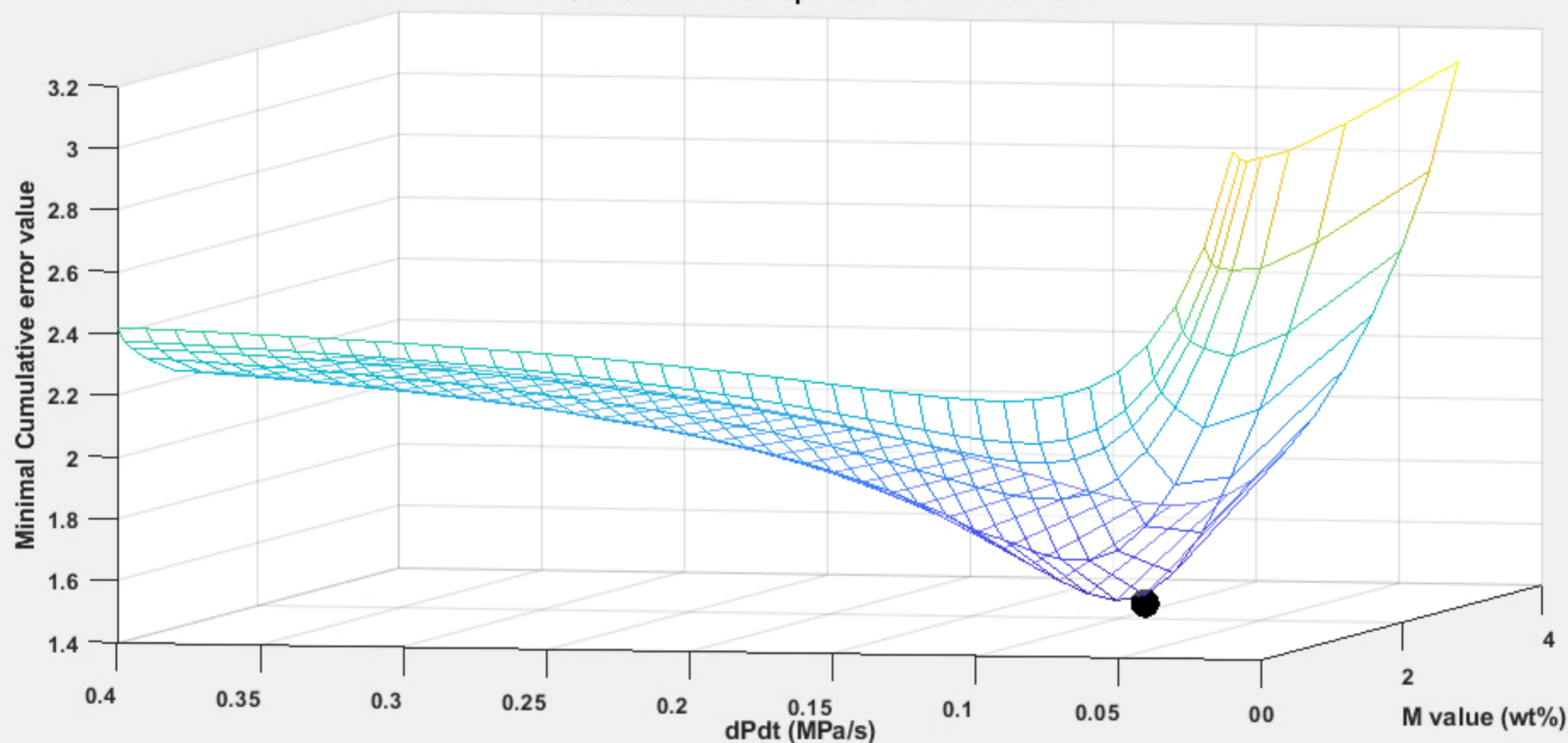
Figure 3.

**a**Comparison of H<sub>2</sub>O-estimated best fits for each M value**b**

Cumulative best fit at 0.08 MPa/s

**c**

Cumulative error repartition over dPdt and M

**d**H<sub>2</sub>O Error repartition over dPdt at M=1.6 wt%CO<sub>2</sub> Error repartition over dPdt at M=3.2 wt%

S Error repartition over dPdt at M=0.2 wt%

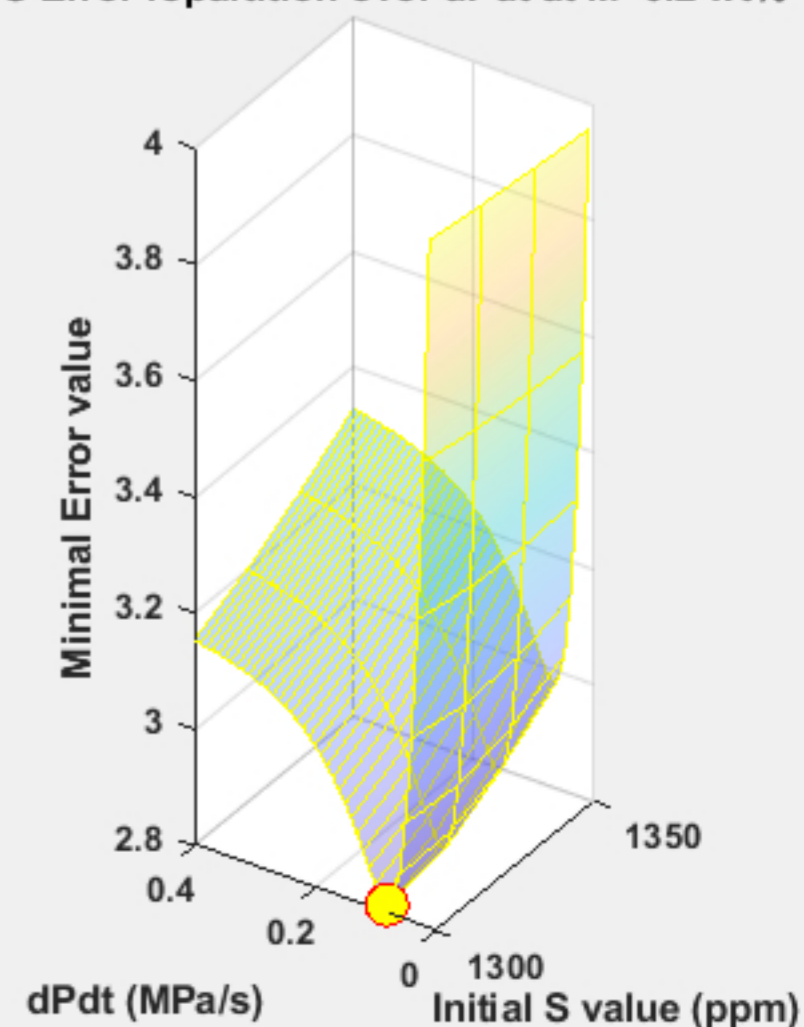
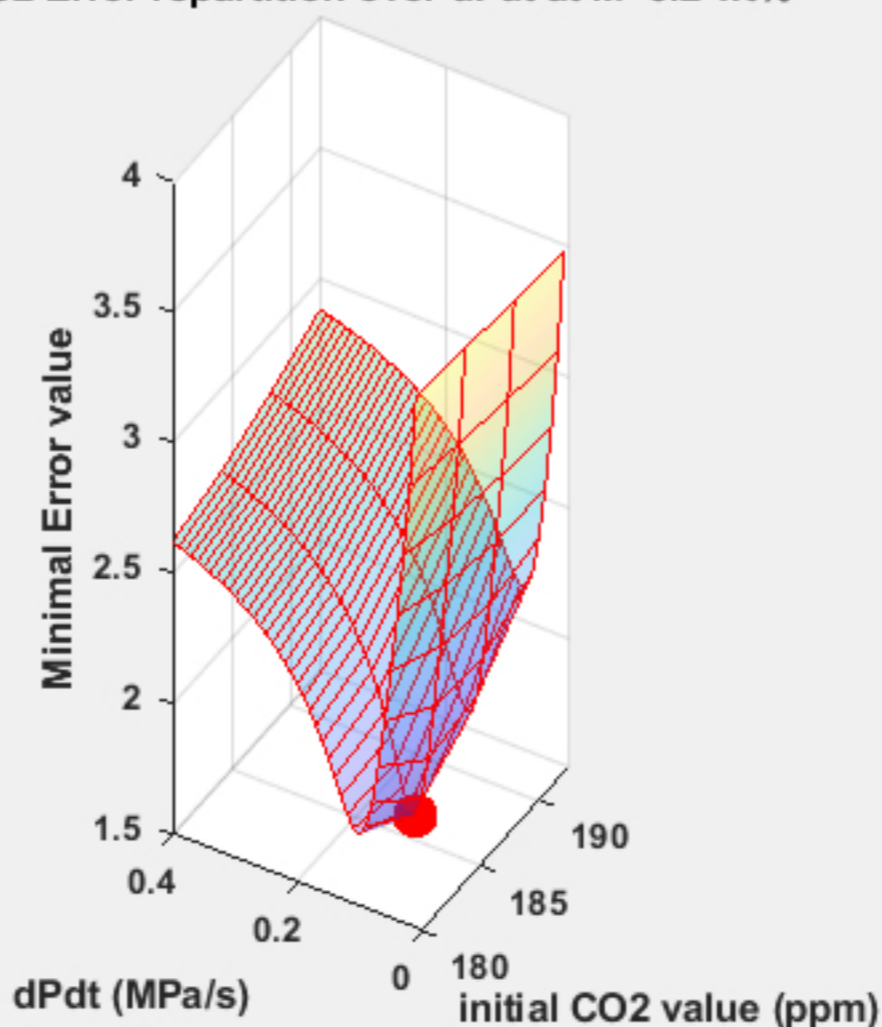
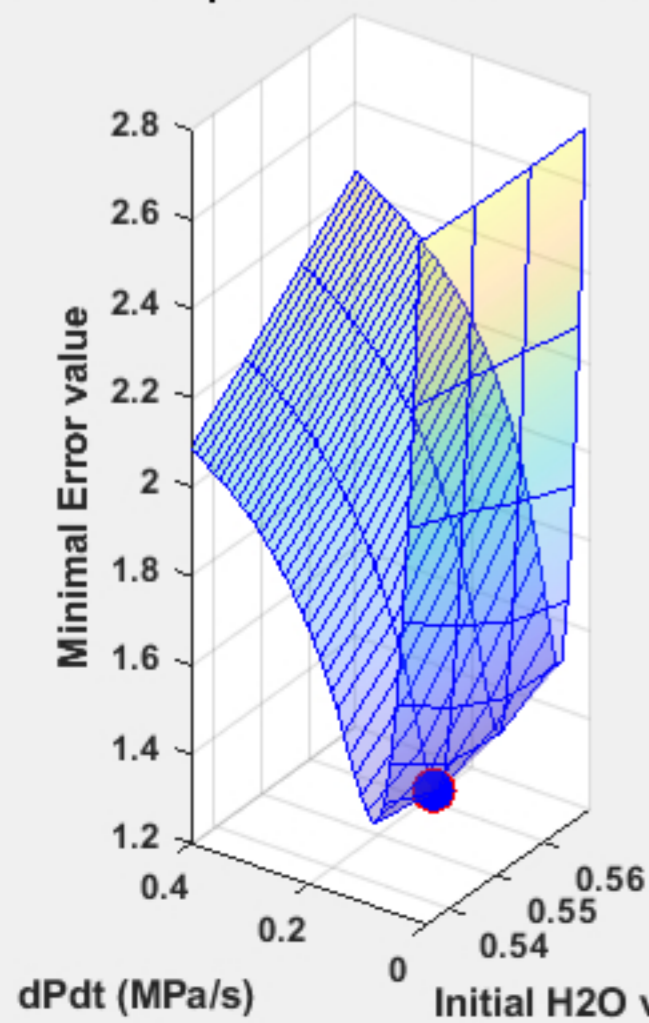


Figure 4.

Decompression rate recalculated with EMBer (MPa/s)

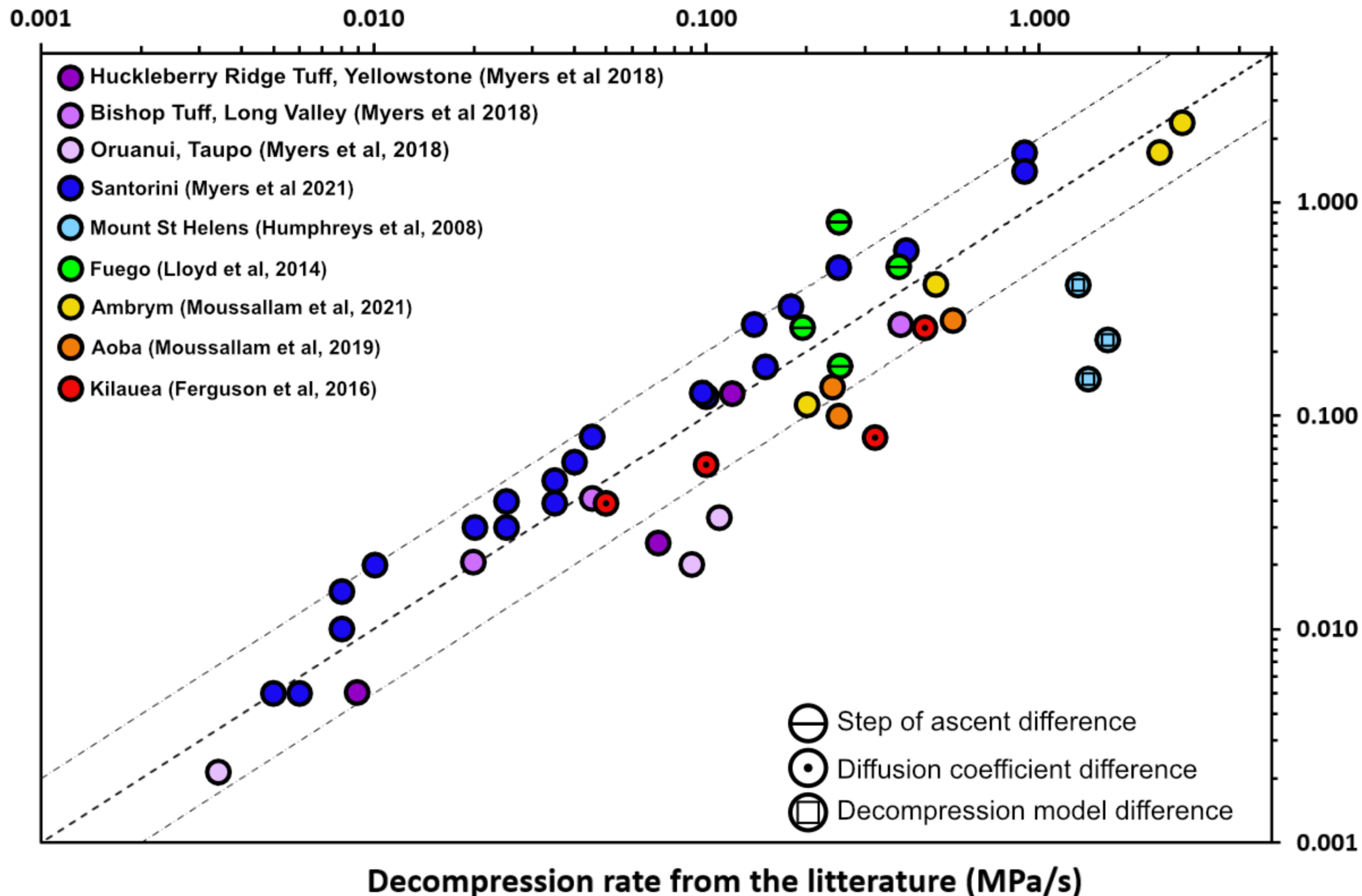
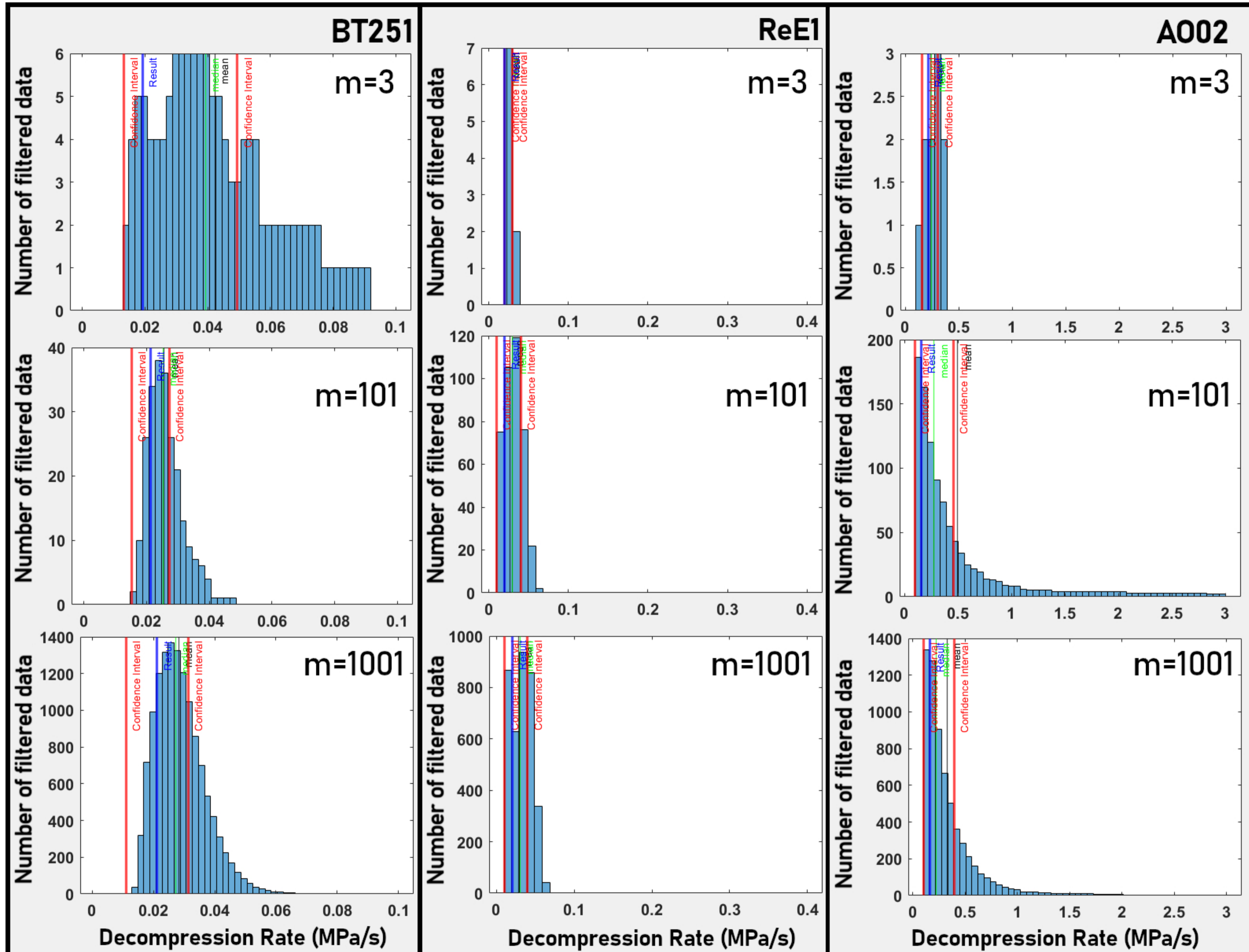


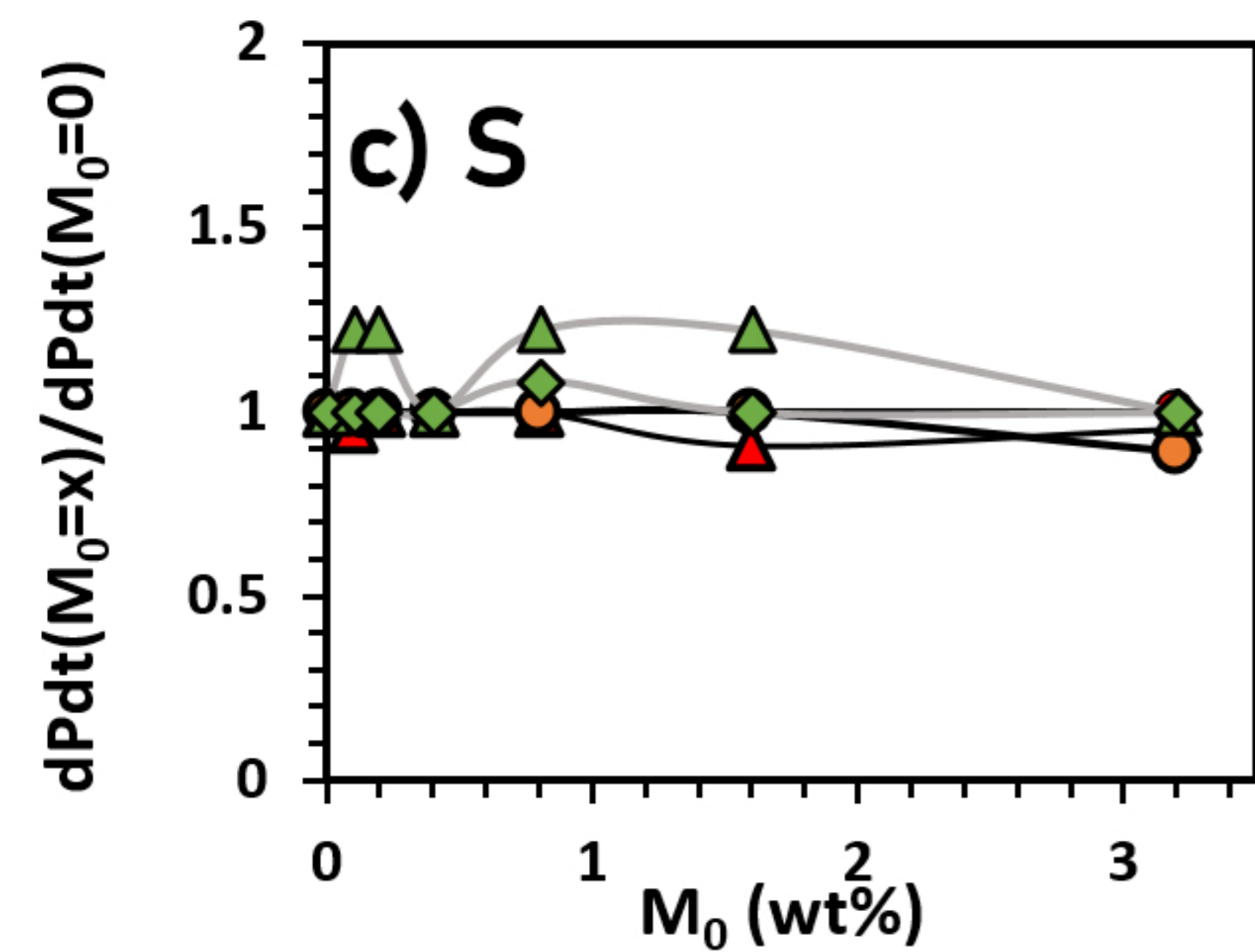
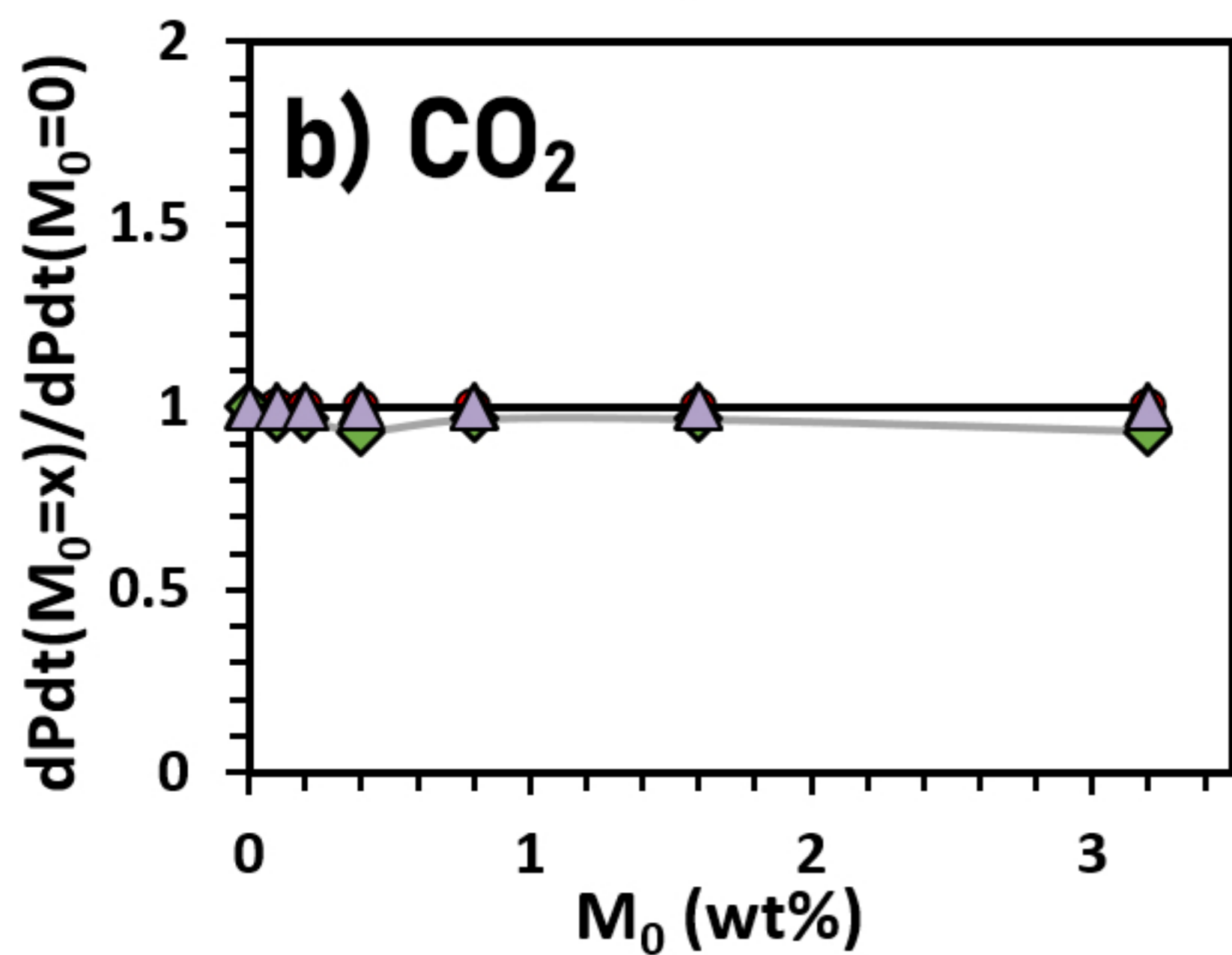
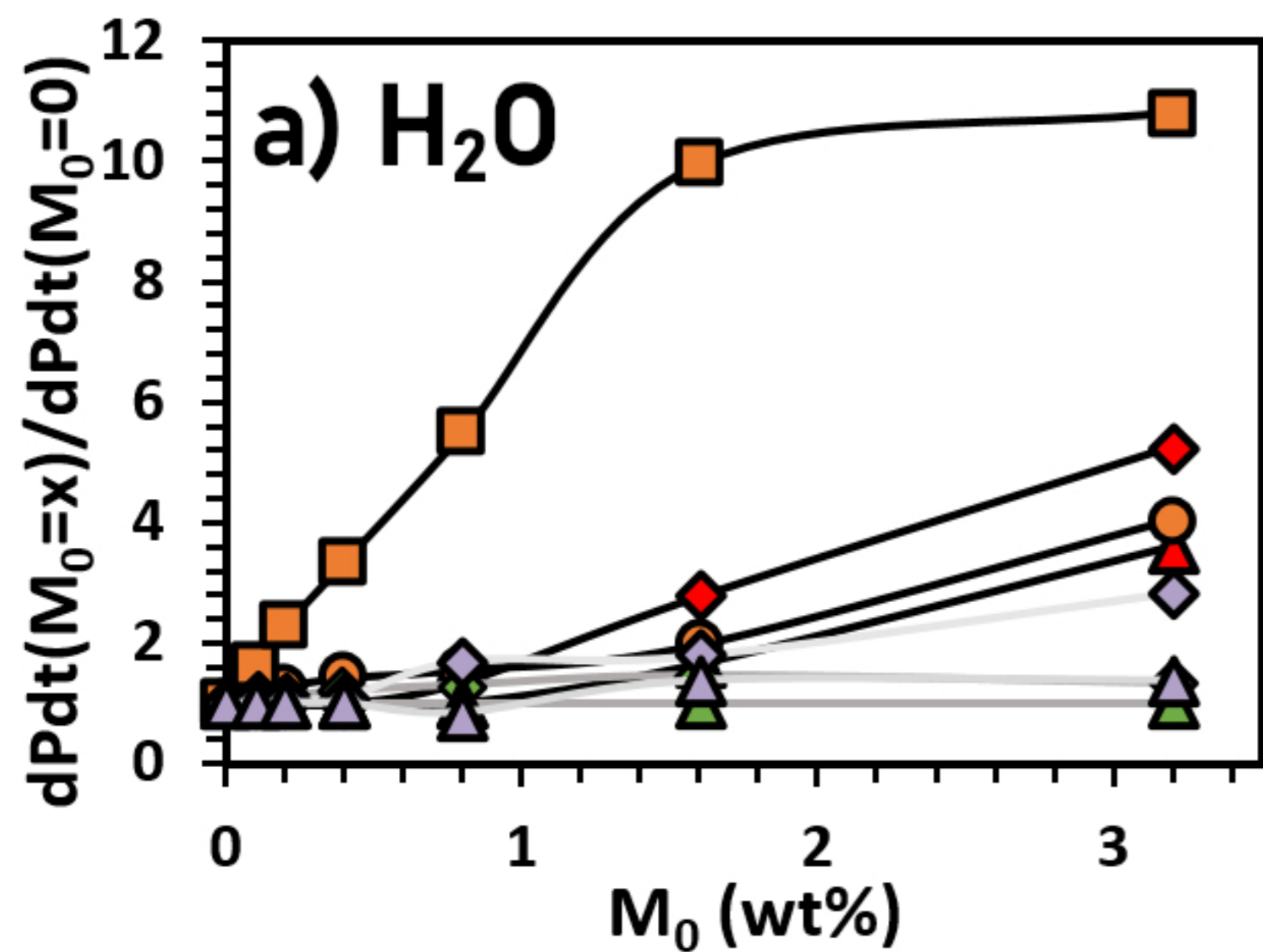
Figure 5.



number of iterations						number of iterations						number of iterations					
BT251	3	11	101	501	1001	ReE1	3	11	101	501	1001	A002	3	11	101	501	1001
Result	0.019	0.021	0.021	0.021	0.021	Result	0.020	0.020	0.020	0.020	0.020	Result	0.218	0.218	0.159	0.159	0.159
Median	0.039	0.023	0.025	0.027	0.027	Median	0.020	0.020	0.030	0.020	0.030	Mean	0.248	0.218	0.278	0.218	0.218
Mean	0.042	0.022	0.026	0.027	0.028	Mean	0.022	0.023	0.027	0.023	0.028	Median	0.236	0.250	0.498	0.287	0.326
Uncertainty	-0.006	-0.004	-0.006	-0.008	-0.01	Uncertainty	-0	-0	-0.01	-0	-0.01	Uncertainty	-0.059	-0.059	-0.059	-0.059	-0.059
	+0.03	+0.004	+0.006	+0.008	+0.01		+0.01	+0.02	+0.02	+0.03	+0.02		+0.089	+0.202	+0.296	+0.178	+0.237

Figure 6.

# M<sub>0</sub> study



# P<sub>end</sub> study

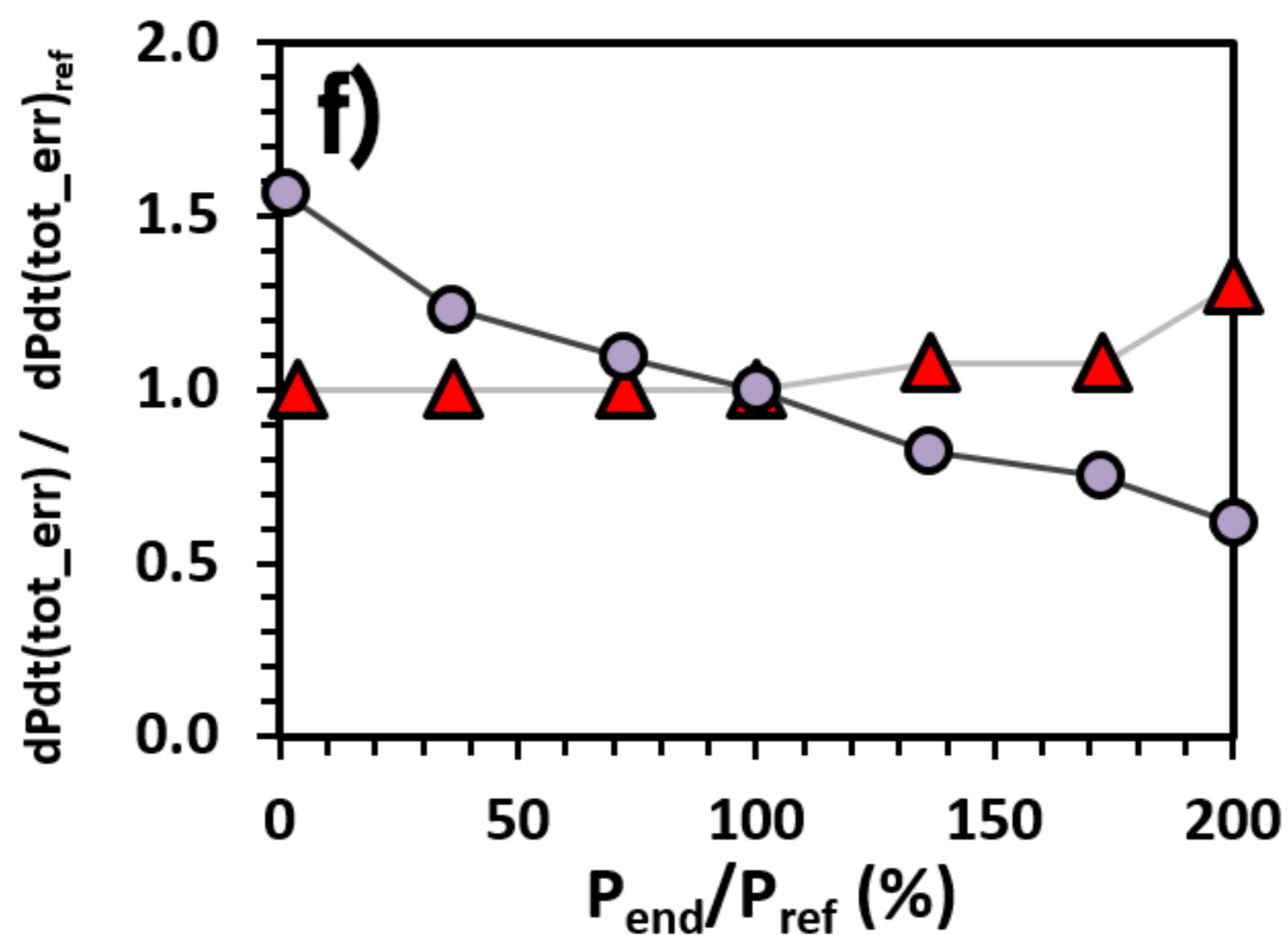
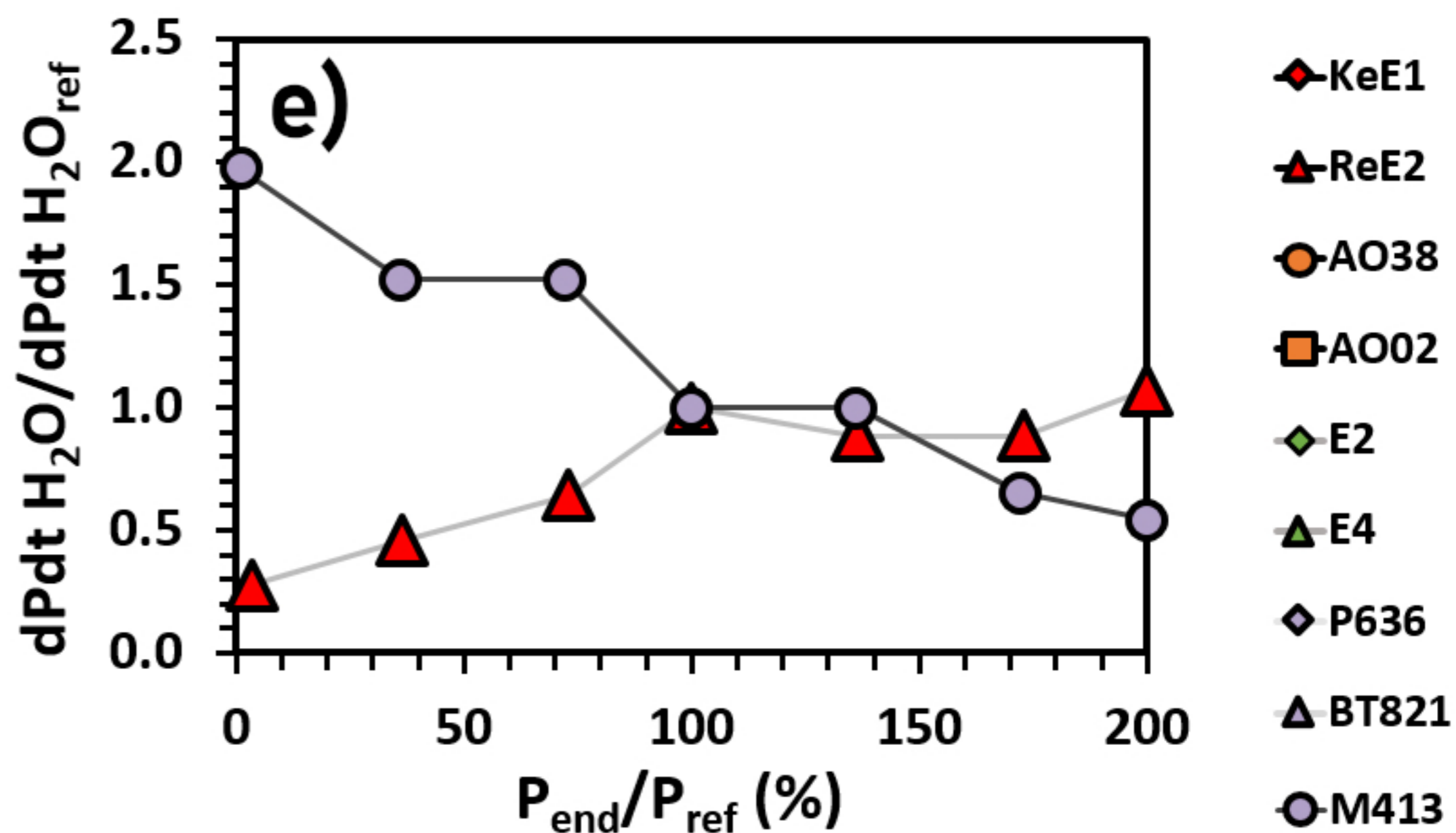
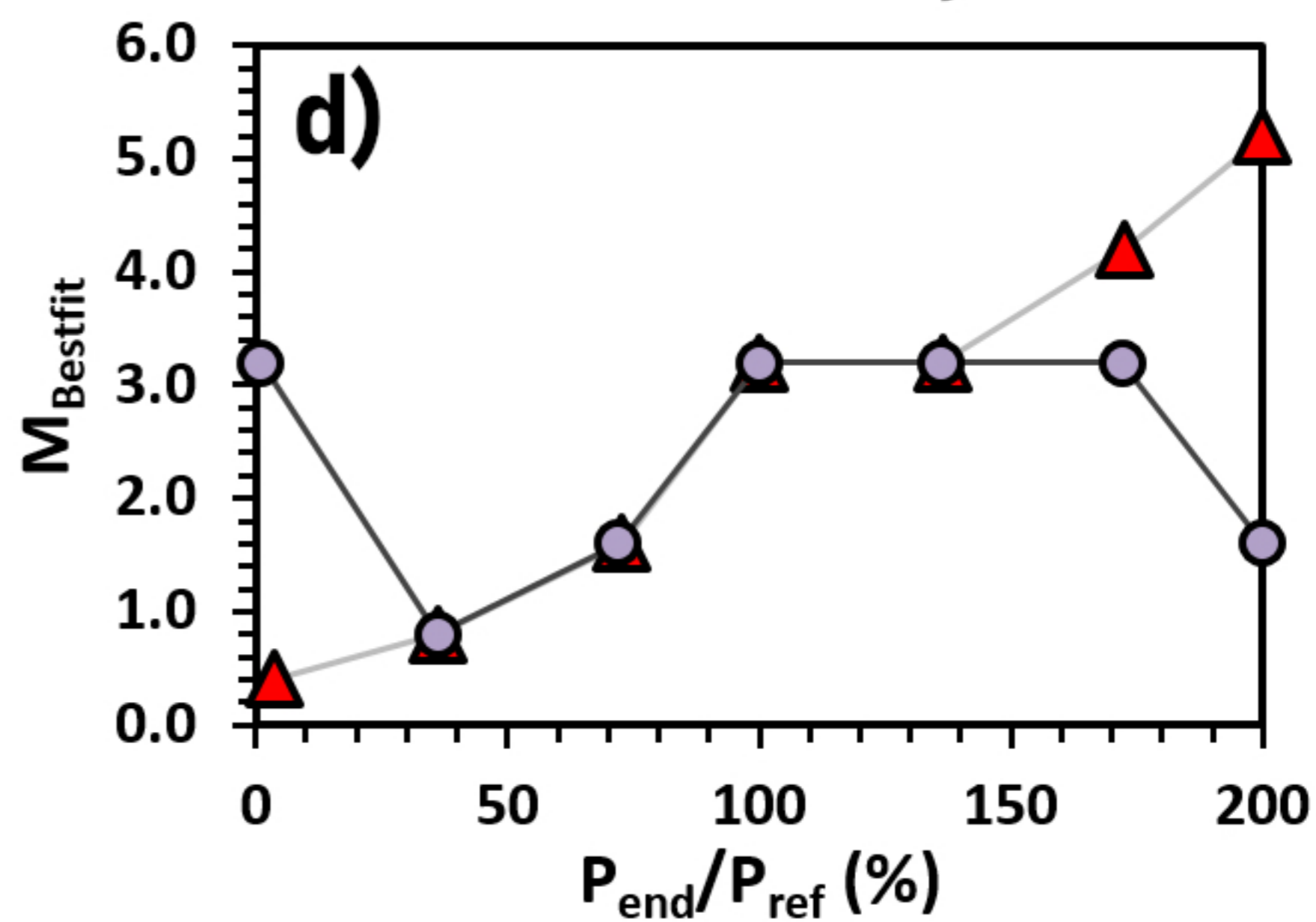


Figure 7.

